Ras-dependent activation of BMAL2 regulates hypoxic metabolism in pancreatic cancer

H. Carlo Maurer[1, 2, 3, *], Alvaro Garcia-Curiel[2, 3, 4, *], Sam R. Holmstrom[5], Cristina Castillo[6, 7, 8], Carmine F. Palermo[2, 3, 4], Steven A. Sastra[2, 3, 4], Anthony Andren[6, 7, 8], Li Zhang[6, 7, 8], Tessa Y.S. Le Large[9, 10], Irina Sagalovskiy[2, 3], Daniel R. Ross[2, 3, 4], Winston Wong[2, 3], Kaitlin Shaw[11], Jeanine Genkinger[12], Gulam A. Manji[2, 3], Alina C. Iuga[13], Roland M. Schmid[1], Kristen Johnson[14], Michael A. Badgley[2 3, 4], Costas A. Lyssiotis[6, 7, 8], Yatrik Shah[6, 7, 8], Andrea Califano[2, 15, 16, 17], and Kenneth P. Olive[2, 3, 4, †]

[1]Department of Internal Medicine II, Klinikum Rechts der Isar, School of Medicine, Technical University of Munich, Munich, Germany
[2]Herbert Irving Comprehensive Cancer Center, Columbia University Irving Medical Center, New York, NY
[3]Department of Medicine, Vagelos College of Physicians and Surgeons, Columbia University, New York, NY
[4]Columbia University Digestive and Liver Disease Research Center, Columbia University Irving Medical Center, New York, NY
[5]Department of Internal Medicine, University of Texas Southwestern Medical Center, Dallas, TX
[6]Department of Molecular & Integrative Physiology and Internal Medicine, Division of Gastroenterology, University of Michigan, Ann Arbor, MI
[6]Department of Internal Medicine, University of Michigan, Ann Arbor, MI
[7]University of Michigan Rogel Cancer Center, University of Michigan, Ann Arbor, MI
[8]Department of Internal Medicine, Division of Gastroenterology and Hepatology, University of Michigan, Ann Arbor, MI
[9]Department of Surgery, Amsterdam UMC, Location Vrije Universiteit, Amsterdam, Netherlands
[10]Cancer Center Amsterdam, Imaging and Biomarkers, Amsterdam, Netherlands
[11]Division of GI/Endocrine Surgery, Department of Surgery, Vagelos College of Physicians and Surgeons, Columbia University, New York, NY
[12]Department of Epidemiology, Mailman School of Public Health, Columbia University, New York, NY
[13]Department of Pathology, Columbia University Irving Medical Center, New York, NY
[14]University of New Hampshire, Manchester, NH
[15]Department of Systems Biology, Vagelos College of Physicians and Surgeons, Columbia University, New York, NY
[16]Darwin Therapeutics, New York, NY
[17]Chan Zuckerberg Biohub, New York, NY
[*]These authors contributed equally to this work
[†]Corresponding author

Summary

To identify drivers of malignancy in human pancreatic ductal adenocarcinoma (PDAC), we performed regulatory network analysis on a large collection of expression profiles from laser capture microdissected samples of PDAC and benign precursors. We discovered that BMAL2 plays a role in the initiation, progression, post resection survival, and KRAS activity in PDAC. Functional analysis of BMAL2 target genes led us to hypothesize that it plays a role in regulating the response to hypoxia, a critical but poorly understood feature of PDAC physiology. Knockout of BMAL2 in multiple human PDAC cell lines revealed effects on viability and invasion, particularly under hypoxic conditions. Loss of BMAL2 also affected glycolysis and other metabolic processes. We found that BMAL2 directly regulates hypoxia-responsive target genes. We also found that BMAL2 is necessary for the stabilization of HIF1A upon exposure to hypoxia, but destabilizes HIF2A under hypoxia. These data demonstrate that BMAL2 is a master transcriptional regulator of hypoxia responses in PDAC and may serve as a long-sought molecular switch that distinguishes HIF1A- and HIF2A-dependent modes of hypoxic metabolism.

Statement of significance

We provide a comprehensive portrait of the molecular drivers behind pancreatic cancer initiation, progression and outcome. We discover a new genetic regulator of metabolic responses to low oxygen environments, a key feature of pancreatic cancer biology. This protein, BMAL2, is a new driver of pancreatic cancer malignancy.

Introduction

DNA sequencing of hundreds of human pancreatic tumors has helped define the genetic drivers of pancreatic ductal adenocarcinoma (PDAC). However, mutations poorly predict key, clinically relevant traits of the disease, such as tumor stage or therapeutic response [1, 2]. This suggests that non-genetic factors may control vital, biological characteristics of PDAC (differentiation state, metastatic potential, progression rate, etc.). Defining these factors will yield an improved understanding of the biological mechanisms that drive this devastating disease.

While RNA sequencing (RNA-Seq) has classically been used to study correlations between gene expression and phenotypes, new techniques in systems biology allow one to use gene expression to infer the causal drivers of phenotypes [3]. Briefly, the activity of transcription factors and other transcriptional regulators (collectively, "regulatory proteins" or RPs) can be calculated from the integrated expression of their target genes using algorithms such as VIPER [4, 5]. By determining the RPs whose targets are most highly activated or repressed between two phenotypes, one can determine the master transcriptional regulators (MRs) that drive those phenotypes [3]. Inhibiting MRs genetically or therapeutically is frequently effective in reversing their associatied phenotypes. This approach is founded on algorithms like ARACNe, which can accurately infer context-specific sets of target genes for each RP on a genome-wide scale using appropriate, context-specific gene expression data [6–8].

Activating mutations in *KRAS* are established as the genetic drivers of nearly all human PDAC tumors and extensive work has delineated the signal transduction pathways that effect its activity. However, there is a comparatively poor understanding of how the downstream transcriptional outputs of mutant *KRAS* drive the overall malignancy of PDAC, including phenotypes such as tumor initiation, tumor progression, and overall survival. We therefore set out to understand how mutant *KRAS* drives malignant phenotypes in PDAC on a more comprehensive scale.

Results

Master regulator analysis of PDAC nominates BMAL2 as a PDAC driver

To link clinical and pathological phenotypes to gene expression data in PDAC, we first augmented our previous collection [9] of RNA-Seq profiles derived from the malignant epithelium of laser-captured, microdissected (LCM) human PDAC to now include a total of 197 adenocarcinomas, 26 low-grade pancreatic intraepithelial neoplasms (PanINs), and 19 low-grade intraductal papillary mucinous neoplasms (IPMNs) [10]. Together, the PanIN and IPMN samples served as "benign controls" that are committed to the neoplastic lineage [11, 12] but unlikely to ever progress to PDAC [10, 13]. Unsupervised clustering by Principal Component Analysis (PCA) showed a clear distinction between precursor and PDAC expression profiles (**Figure 1A**).

To benchmark the dataset, we conducted an unbiased analysis of associations between gene expression and histopathological features, as drawn from observations of adjacent tissue sections (**Supplementary Figure S1A**). We found, for example, poorly differentiated tumors had elevated expression of *KRAS* [14, 15], of proliferation markers (*TOP2A*, *BUB1B*, *CDC20*, and *TK1*) [16], and indicators of squamous PDAC lineage (*KRT5*, *KRT6A*, *PTHLH*, and *S100A2*) [17, 18] (**Figure 1B**). Conversely, hallmarks of differentiation (*MUC1*, *MUC5AC*) and GI lineage (*TFF1*, *TFF2*) decreased during tumor initiation and progression, providing strong validation for these established biomarkers.

While the correlations identified through differential gene expression analysis can yield some insights, regulatory network analysis provides a means to connect phenotypes to their mechanistic drivers. Briefly, this approach generates a tissue-specific list of the positive and negative target genes for each of thousands of transcription factors, co-factors, and other regulatory proteins (i.e. a regulatory network). With this information, one can calculate the relative activity of each regulatory protein within a single sample by integrating the expression of the protein's target genes. This makes it possible to determine which regulatory proteins are most differentially activated or repressed between groups of samples that exemplify a phenotype – that is, the master transcriptional regulators whose activities drive (or repress) that phenotype. This approach has been extensively validated in numerous systems [4, 6, 8, 19, 20].

To implement regulatory network analysis to study PDAC malignancy, we first applied ARACNe [4, 5] to the full set of 242 epithelial expression profiles to generate a regulatory network specific to PDAC epithelia. This analysis compiled 263,085 inferred transcriptional targets for 2,211 regulatory proteins (RP). For 26 of these RPs, ChIP-Seq data were publicly available in human PDAC cells [21]. Half of these (13/26) showed a significant overlap with the ARACNe target gene sets, despite the difference of *in vivo* versus *in vitro* contexts (**Supplementary Figure S1B**), providing experimental validation for the accuracy of the regulatory network.

Finally, in order to benchmark the regulatory network to established PDAC biology, we examined the inferred activities of proteins with well-studied roles in PDAC (**Figure 1C**). Principal component 1 (PC1) effectively captured the progression from benign precursors through low-grade PDAC, to high-grade PDAC with squamous features. These phenotypic changes were accompanied by the repression of canonical PDAC tumor suppressors TP53 and SMAD4, and activation of RPs with known oncogenic functions in PDAC, such as FOXA1 [22] and TRIM29 [23] (**Figure 1C**). GI transcription factors GATA6, FOXA2, and

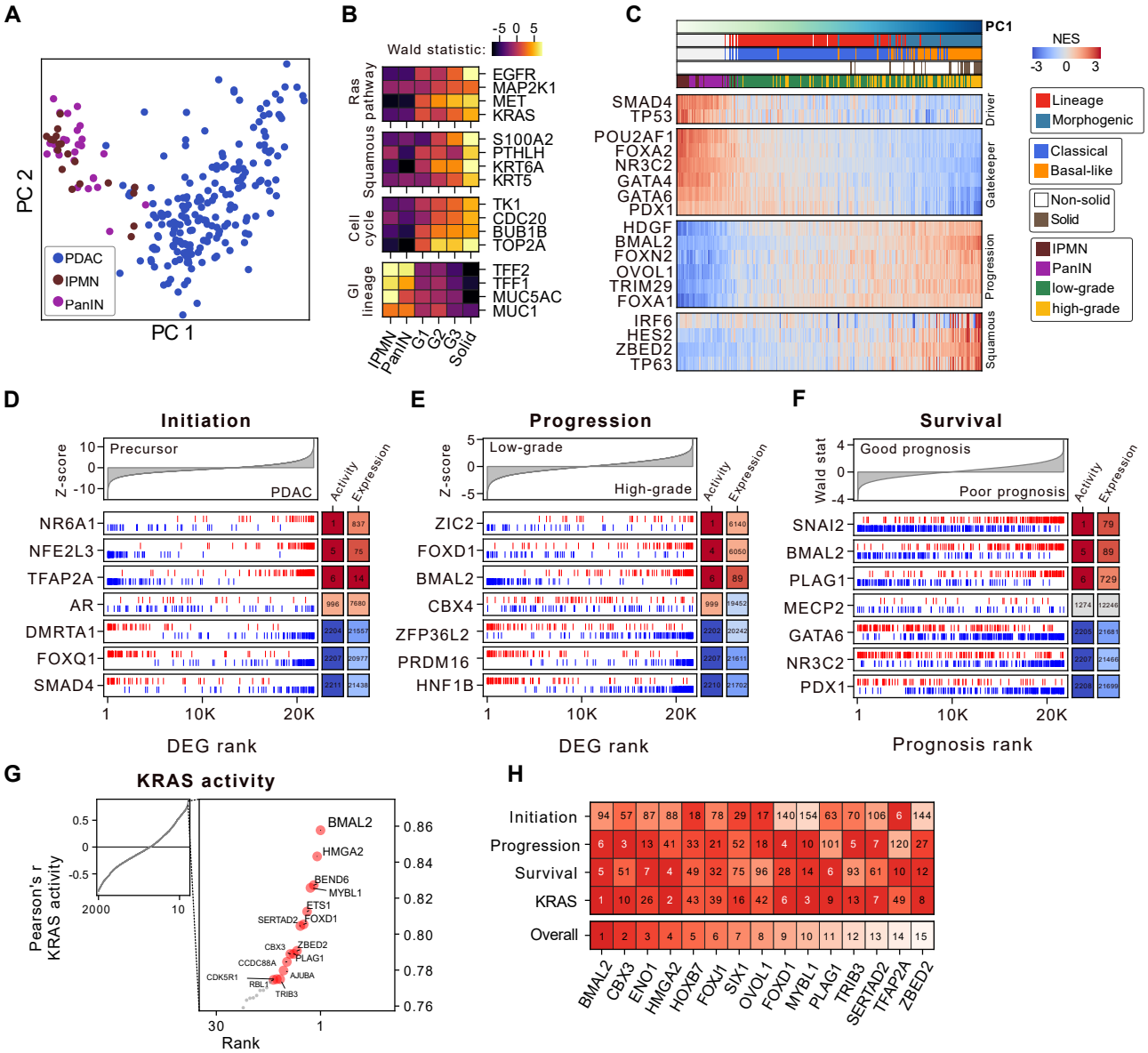

Figure 1: (**A**) Principal component analysis (PCA) of precursor and PDAC LCM RNA-Seq samples used to assemble a regulatory model (interactome) of PDAC carcinogenesis. (**B**) Heatmap depicting select differentially expressed genes between the indicated histopathological groups (x-axis). Wald test statistics were derived from a negative-binomial linear model comparing the respective group against all other groups. (**C**) Heatmap of protein activity scores (NES) for select regulatory proteins during PDAC progression. The samples are ordered by their value in the first principal component, essentially capturing progression and dedifferentiation. (**D**) Select results from master regulator analysis on a genome-wide PDAC initiation gene expression signature (x-axis) represented by Z-scores for each gene. Each regulatory protein's regulon is represented by red (positive targets) and blue (negative targets) vertical bars. The rank of each RP based on activity and expression, respectively, is illustrated on the right. (**E**) Select results from master regulator analysis on a genome-wide PDAC progression gene expression signature (x-axis) (**F**)) Select results from master regulator analysis on a genome-wide survival signature (x-axis) represented by Wald test statistics from a multivariate Cox Proportional Hazards model testing the coefficient for each gene's continuous expression while accounting for patient age (**G**) Genome-wide Pearson correlation between KRAS and RP activity with illustration of the most positively correlated RPs (**H**) Heatmap of rank positions for the indicated regulatory proteins (x-axis) in each of four critical phenotypic PDAC transitions yields a conserved core set of non-oncogene dependency candidates for PDAC. A low rank represents activation in a given phenotype signature.

PDX1, which have been described as being "overexpressed" in some PDAC molecular subtypes [15, 24], were indeed shown to be more highly active in low-grade PDAC than in high grade. However, in comparison to benign precursors, their activity in low-grade tumors was down-regulated, consistent with an overall loss of GI identity during tumor initiation and progression. Finally, drivers of squamous histology such as TP63 [17] and ZBED2 [25] were hyperactivated in high-grade PDAC, particularly those with annotated squamous histology.

Next, we identified regulatory drivers of PDAC malignancy by identifying the RPs whose activities were most strongly associated with four key malignant phenotypes: tumor initiation, tumor progression, patient survival, and KRAS signaling activity (**Supplementary Figure 1C**). We used MARINa analysis [26] to identify MRs of PDAC initiation (comparing precursors to adenocarcinoma, **Figure 1D**) and progression (comparing PDAC with low-grade versus high-grade histopathology, **Figure 1E**). For survival, we constructed a survival signature from a multivariate Cox proportional hazards model and identified RPs controlling the expression of the most prognostic target genes (**Figure 1F**). Finally, we calculated KRAS activity by iterating a new PDAC regulatory network comprising the transcriptional targets for a total of 2,523 signaling factors (see Methods). In this analysis, the inferred target genes of each signaling protein serve as a bespoke reporter gene set, providing an indirect, but unbiased, measure of its signaling activity in PDAC [7, 27]. As expected, the inferred activity of KRAS increased significantly during tumor initiation and tumor progression (**Supplementary Figure 1D**), peaking among tumors growing in solid nests.

To better understand the genetic programs and molecular systems underpinning each phenotype, we annotated the transcriptional targets controlled by the top RPs using HALLMARK gene sets (**Supplementary Figure S1E**). For example, the RPs of PDAC initiation and progression broadly regulated gene sets associated with a wide range of proliferative and pro-tumorigenic processes. Notably, top MRs of patient survival were associated with processes such as hypoxia, KRAS signaling, immune signaling, and EMT, but not with proliferation, suggesting that differences in the survival of PDAC patients do not necessarily correlate with tumor growth rate [35]. Finally, we integrated the results of all four analyses and found that BMAL2, a member of the PAS superfamily, is the top candidate master transcriptional regulator of PDAC malignancy (**Figure 1H**).

BMAL2 is associated with aggressiveness in multiple PDAC datasets

Given that BMAL2 has not previously been indicated as a key driver of PDAC, we assessed the reproducibility of our findings across multiple multiple external datasets. We performed a meta-analysis across a total of 10 published PDAC expression studies [24, 36–44] and found that *BMAL2* expression was elevated relative to normal pancreas (**Supplementary Figure S2A**) and elevated in high-grade tumors versus low-grade PDAC specimens (**Supplementary Figure S2B**). Concordant with our findings in the CUMC cohort, high BMAL2 activity, but not expression, consistently identified patients with worse outcomes (**Supplementary Figure S2C**). Next, we evaluated each combination of five subtype classification schemes and six PDAC expression data sets for differences in BMAL2 activity between tumors of the most aggressive versus least aggressive subtype (**Supplementary Figure S2D**), and found that BMAL2 was consistently hyperactivated in the most aggressive subtype [45–47].

Finally, we found *BMAL2* expression in normal tissues (**Supplementary Figure S2E**) [45] to be highest in squamous epithelia, whereas expression in the normal pancreas was comparatively low. By contrast, PDAC tumor samples had among the highest levels of *BMAL2* expression across multiple cancers (**Supplementary Fig. S2F**) [46] and PDAC cell lines had the highest median expression across cell lines from different lineages [47] (**Supplementary Figure S2G**). Together these results support our analysis identifying BMAL2 as a key driver of initiation, progression, and outcome in multiple independent PDAC datasets.

Oncogenic KRAS activates BMAL2 via the ERK mitogen-activated protein kinase cascade

While BMAL2 emerged as a regulator of all four of the phenotypes studied, it stood out as the single RP that was most highly associated with KRAS activity. Given the role of mutant *KRAS* as a driver of PDAC, we sought to test the KRAS dependency of BMAL2 experimentally. We identified published expression datasets in which mutant KRAS activity had been modulated: $Kras^{G12D}$ reactivation in PDAC cells that survived mutant *Kras* withdrawal (Viale); $Kras^{G12D}$ activation in murine pancreatic ductal cells (Sivakumar, Diersch); and mutant *Kras* inactivation in murine and human PDAC cells (Ying, Bryant) [28–32]. In all five independent experiments, BMAL2 activity was associated with KRAS activation, suggesting that BMAL2 operates downstream of mutant KRAS and relays its transcriptional inputs (**Figure 2A**).

To explore this possibility and further dissect the pathways that regulate BMAL2, we leveraged results from a recent analysis that presented high throughput RNA-Seq data from two human PDAC cell lines treated with 322 different FDA-approved or investigational agents [33, 34] (**Figure 2B**). This exercise revealed a strong overrepresentation of MEK inhibitors among the agents most capable of reducing BMAL2 activity in PDAC lines (**Figure 2C**). By contrast, we did not observe effects of this magnitude

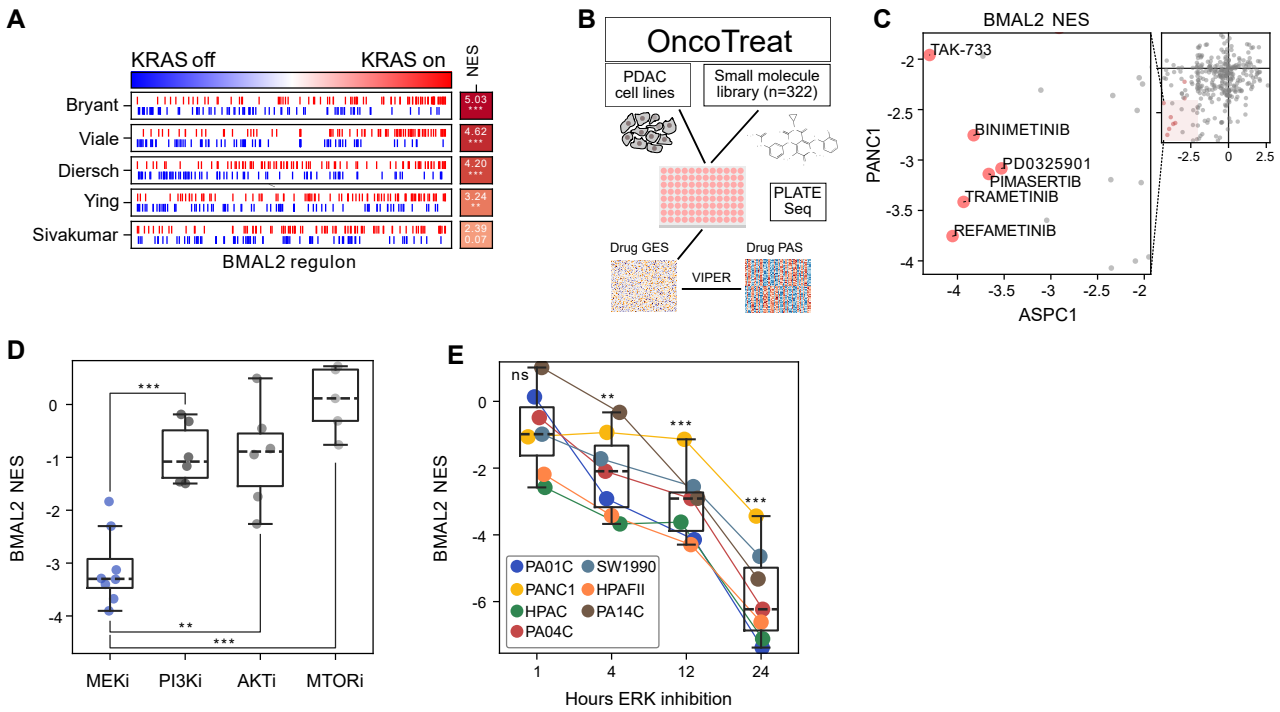

Figure 2: (**A**) BMAL2 regulon enrichment in the indicated genome-wide gene expression signatures in response to oncogenic *Kras* mutation (Refs. [28–32]). Positive and negative targets, respectively, are represented by red and blue vertical bars, respectively. Normalized enrichment score (NES) and p-values are calculated by two-tailed analytic rank-based enrichment analysis (aREA, p-values are Bonferroni corrected) (**B**) Schematic of the experimental design to study the effect of a library of antineoplastic compounds on regulatory protein activity as part of the OncoTreat framework (Refs. [33, 34]) (**C**) Effects of 322 antineoplastic compounds on BMAL2 activity (NES) in ASPC1 (x-axis) and PANC1 (y-axis) cells. Zoomed area shows compounds with consistent and potent reversal of BMAL2 activity. Red circles mark MEK inhibitors, all other compounds are grey. (**D**) Reversal of BMAL2 activity (y-axis, normalized enrichment score, NES) for the indicated compound classes (x-axis). P-values are derived from pairwise t-tests with posthoc Bonferroni correction. (**E**) Reversal of BMAL2 activity (y-axis, NES) at the indicated time points of treatment with an ERK inhibitor (SCH772984) in 7 PDAC cell lines. P-values are derived from one-sample, two-tailed t-tests with Bonferroni correction. **: $p \leq 0.01$, ***: $p \leq 0.001$, ns: not significant. In boxplots, the box ranges from Q1 (the first quartile) to Q3 (the third quartile) of the distribution and the range represents the IQR (interquartile range). The median is indicated by a dashed line across the box. The "whiskers" on box plots extend from Q1 and Q3 to 1.5 times the IQR.

for inhibitors of other KRAS effector proteins, including PI3K, AKT, and MTOR (**Figure 2D**). Although this screen lacked ERK inhibitors, a reanalysis of experimental expression data from PDAC cells treated with the ERK1/ERK2-selective inhibitor SCH772984 found decreasing BMAL2 activity over the course of 24 hours [31] (**Figure 2E**). Together, these findings suggest that BMAL2 receives input from oncogenic *KRAS* via the RAF/MEK/ERK effector pathway.

The bHLH-PAS family member BMAL2 controls hypoxia response targets

BMAL2 belongs to the helix–loop–helix-PER-ARNT-SIM (bHLH-PAS) family of transcription factors that heterodimerize to drive functions such as circadian rhythm programs, innate and adaptive immune responses, oxygen-sensing mechanisms, and response to deleterious environmental exposures [49]. BMAL2 is classically associated with circadian processes, serving as a binding partner for CLOCK [50, 51], but sequence conservation analysis shows that BMAL1 and BMAL2 are most closely related to ARNT (HIF1B) and ARNT2 (HIF2B), the binding partners of HIF1A (**Figure 3A**). We therefore undertook a systematic assessment of bHLH-PAS family member activity and transcriptional hypoxia scores [52] for each of our 197 tumor profiles and found BMAL2 to exhibit the highest average positive correlation (Spearman's rho 0.46, **Figure 3B**). Surprisingly, neither HIF1A nor HIF1B (ARNT) were strongly correlated with hypoxia signatures in PDAC epithelial samples, despite being among the top correlated PAS family members in laser capture microdissected PDAC stromal samples (N=124, **Supplementary Figure S3A**). Using bespoke regulatory networks for multiple tumor types across TCGA datasets, BMAL2 was frequently among the most hypoxia-associated bHLH-PAS family members, along with HIF1A and HIF1B (**Supplementary Figure S3B**), suggesting that BMAL2 may play an underappreciated role in the hypoxia responses across human tumors. Next, we analyzed the PDAC regulatory network to assess whether BMAL2 could directly or indirectly regulate genes canonically regulated by HIF1A [48] and found that BMAL2 impacts 33 out of 44 hypoxia genes in a net positive manner, including

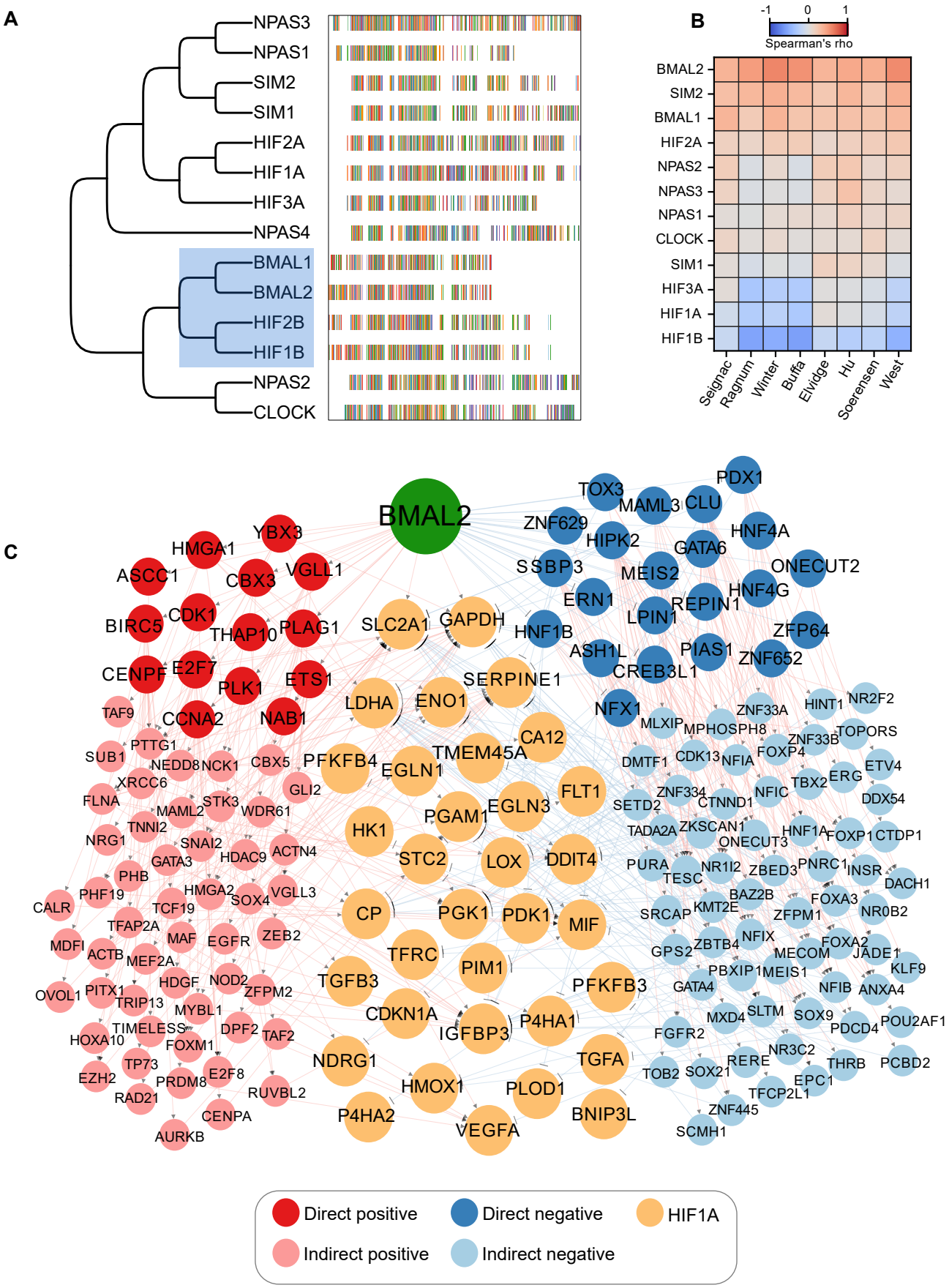

Figure 3: (**A**) Phylogenetic tree illustrating the pairwise distance based on sequence alignment of bHLH-PAS family transcription factors. Blue rectangle highlights the closest family members for BMAL2. Vertical bars represent specific amino acids at the indicated position (1-1300). (**B**) Heatmap of Spearman's rank correlation between transcriptional hypoxia scores using signatures from the indicated references (x-axis) and epithelial protein activity for bHLH-PAS family members (y-axis). (**C**) HIF target genes (Ref. [48], orange) controlled directly or indirectly by BMAL2 (green). Indirect control involves both BMAL2's negative influence on first (dark blue) or second tier (light blue) RP repressing HIF target genes, and positive influence on first (dark red) and second (light red) tier RP activating HIF target genes.

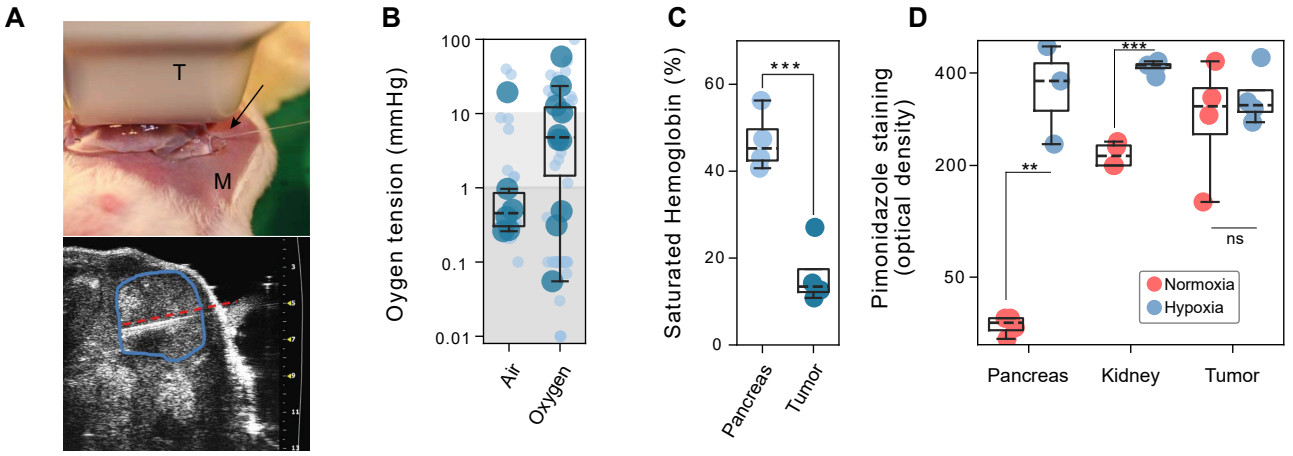

Figure 4: (**A**) Image (top) shows a KPC mouse (M) being imaged with an ultrasound transducer (T), with percutaneous insertion of the OxyLite probe (arrow). An ultrasound image (bottom) shows the probe (red hashline, offset) extending through the abdominal wall and through the depth of the tumor (outlined in blue). (**B**) Oxygen tension (y-axis) as determined by an OxyLite probe in tumors from KPC mice breathing ambient air or pure oxygen (x-axis). Dark blue circles represent averages per tumor and boxplots illustrate their distribution. Light blue circles represent repeat measurements per tumor at different sites. (**C**) Fraction of saturated hemoglobin (y-axis) in the indicated tissue (x-axis). (**D**) Hypoxia marker pimonidazole staining intensity in the indicated tissues and oxygen conditions. **: $p \leq 0.01$, ***: $p \leq 0.001$, ns: not significant. In boxplots, the box ranges from Q1 (the first quartile) to Q3 (the third quartile) of the distribution and the range represents the IQR (interquartile range). The median is indicated by a dashed line across the box. The "whiskers" on box plots extend from Q1 and Q3 to 1.5 times the IQR.

metabolic proteins such as SLC2A1 (GLUT1), GAPDH and LDHA (**Figure 3C**); none of the canonical HIF1A target genes were regulated by BMAL2 in a net negative manner. Together, these analyses provide a strong basis to hypothesize that BMAL2 plays a role in the adaption of malignant PDAC epithelial cells to low oxygen levels.

Severe hypoxia in pancreatic tumors is highlighted by multiple methods

PDAC tumors are widely considered to be hypoxic due to their poor vascularity and low perfusion [53], but there are few examples of direct *in vivo* measurements of oxygen levels in PDAC tissue. Oxygen microelectrode measurements on a small set of human PDAC patients previously indicated the presence of extreme hypoxia (ranging from 0 – 5.3 mmHg) [54], but technical concerns limited interpretation [55]. To assess whether this extreme range of hypoxia could feasibly reflect the biology of PDAC (and thereby the importance of BMAL2 in these tumors), we measured hypoxia through multiple independent techniques in pancreatic tumors arising in *LSL-Kras*$^{G12D/+}$;*LSL-Trp53*$^{R172H/+}$;*Pdx1-Cre* (KPC) mice – a model system widely utilized for its physiological accuracy to human PDAC. We first performed direct measurements of intratumoral partial oxygen pressure (pO2) using an OxyLite sensor (a gold-standard physical oxygen probe) and found that pO2 levels were <1mmHg in KPC mouse pancreatic tumors (**Figure 4A, B**), reflecting a setting of extreme hypoxia. This finding was further supported via photoacoustic imaging on KPC pancreatic tumors, which revealed an average hemoglobin saturation of just 17%, significantly lower than in adjacent pancreas tissue (**Figure 4C and Supplementary Figures 4A-B**). Finally, we measured activation of the hypoxia probe pimonidazole [56] following its administration to KPC mice respiring normoxic or hypoxia air. In these mice, normal tissues showed marker staining upon exposure to hypoxia whereas PDAC tissues showed equally high levels of staining under both normoxic and hypoxic conditions (**Figure 4D, Supplementary Figure S4C**). Together these experiments demonstrate that autochthonous pancreatic tumors in a physiologically relevant model system naturally exist in a state of extreme hypoxia, underscoring the importance of hypoxia response programs to PDAC biology.

BMAL2-deficient pancreatic cancer cells exhibit enhanced phenotypes in hypoxic environments

To directly test whether BMAL2 plays a role in the hypoxia response of PDAC cells, we examined the effect of BMAL2 loss in four human PDAC cell lines (KP4, PANC1, MIAPACA2, and PATU8902) under both normoxic and hypoxic conditions, using CRISPR/Cas9 genome editing. We observed that cell proliferation was significantly impaired in *BMAL2* knockout cells, in both normoxic and hypoxic environments, across all four cell lines (**Figure 5A**). Using a transwell migration assay, we found that both hypoxia and *BMAL2* knockout led to significant decreases in cell migration compared to non-targeting (sgNT) controls (**Figure 5B**). Importantly, the negative effect of BMAL2 loss on migration was significantly greater under hypoxic conditions than in normoxia ($p_{interaction}$: 0.004), highlighting a specific contribution of BMAL2 to the hypoxia re-

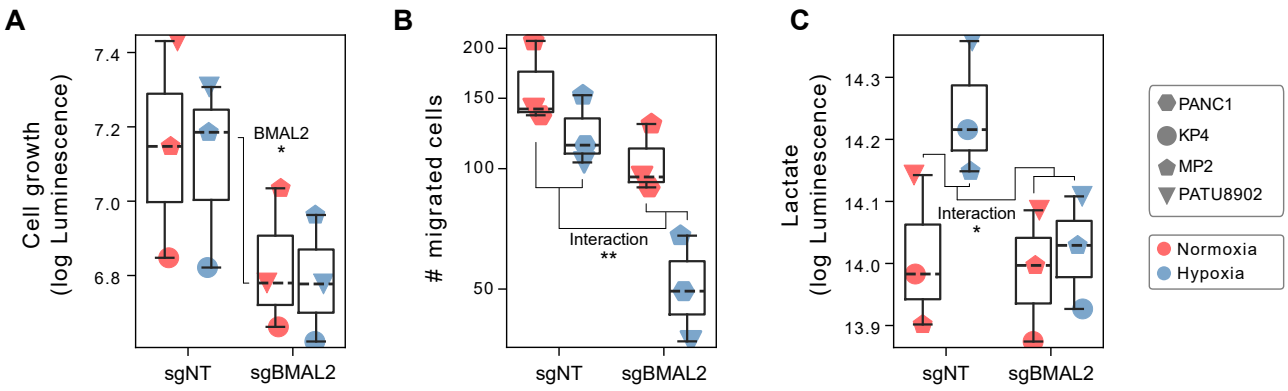

Figure 5: (**A**) Cell numbers represented by luminescence in pancreatic cancer cells expressing non-targeting (sgNT) or *BMAL2*-directed sgRNA (sgBMAL2) in the indicated oxygen environment and cell line. (**B**) Number of migrated cells for pancreatic cancer cells expressing sgNT or sgBMAL2 in the indicated oxygen environment and cell line. P-value stems from testing the interaction coefficient between BMAL2 knockout and hypoxic conditions from a log linear regression model. (**C**) Extracellular lactate levels after 5 days in pancreatic cancer cells expressing sgNT or sgBMAL2 in the indicated oxygen environment and cell line. P-value stems from testing the interaction coefficient between BMAL2 knockout and hypoxic conditions from a log linear regression model. *: $p \leq 0.05$, **: $p \leq 0.01$. In boxplots, the box ranges from Q1 (the first quartile) to Q3 (the third quartile) of the distribution and the range represents the IQR (interquartile range). The median is indicated by a dashed line across the box. The "whiskers" on box plots extend from Q1 and Q3 to 1.5 times the IQR.

sponse of PDAC cells.

A key component of hypoxic metabolism in all cells is the production and secretion of the glycolytic product lactate [57]. We examined the metabolic consequences of *BMAL2* knockout by measuring extracellular lactate levels after five days. As expected, exposure to hypoxia significantly increased extracellular lactate levels. However, this effect was entirely lost in *BMAL2* knockout cells (**Figure 5C**, $p_{interaction}$: 0.025), indicating a strong reliance of glycolysis in PDAC cells on the function of BMAL2. Together these findings highlight a potent impact of BMAL2 loss on cellular phenotypes and they suggest the potential for an outsized effect on hypoxic metabolism.

BMAL2 knockout blunts the transcriptional and metabolic hypoxia response

To better understand the molecular consequences of BMAL2 loss in PDAC cells, we performed transcriptomic and metabolomic profiling of KP4 and MIAPACA2 cells from hypoxic and normoxic environments. Unsupervised clustering of gene expression profiles showed that hypoxia exposure and *BMAL2* knockout dominated the global variance in both cell lines (**Figure 6A**). Compared to their normoxic reference, both hypoxic *BMAL2* knockout and wildtype cells exhibited a substantial increase in known hypoxia-inducible transcripts (**Figure 6B**), indicating that BMAL2 knockout cells are still capable of mounting a transcriptional hypoxia response. However, hypoxia responses were significantly blunted upon loss of BMAL2 in both cell lines (**Figure 6C**). Moreover, we found that 19 out of our 44 hypoxia genes had heterogeneous behavior ($FDR_{interaction} < 0.05$) upon hypoxia exposure depending on whether BMAL2 was perturbed or not (**Figure 6D**).

Similar to the gene expression results, differences in the abundance of about 230 metabolites separated hypoxic from normoxic and *BMAL2* knockout from wildtype cells in a Principal Component Analysis (PCA) (**Figure 6E**). Guided by our transcriptional findings, we focused on metabolites that increased in hypoxic conditions but to a lesser degree in *BMAL2* knockout cells compared to wildtype cells (**Figure 6F**). Among these, metabolite set analysis found significant overrepresentation of metabolites from glycolysis and related metabolic pathways (**Figure 6G**) including fructose 6-phosphate, fructose 1,6-bisphosphate, and glyceraldehyde 3-phosphate (G3P). Together these results indicate that both the transcriptional and metabolic responses to hypoxia in PDAC cells are significantly blunted upon loss of BMAL2.

HIF1A-BMAL2 interaction reveals oxygen-dependent stabilization in pancreatic cancer cells

We next sought to understand the mechanism(s) by which BMAL2 modulates hypoxia responses. Given the structure of BMAL2, we first evaluated interactions with HIF1A and HIF2A, as well as LDHA. Western Blot analysis on PANC1 cells revealed dynamic changes in the expression levels of HIF1A, HIF2A, and BMAL2, with pronounced alterations in response to oxygen availability (**Figure 7A**). Notably, HIF1A stabilization in hypoxic conditions exhibited a distinct dependence on BMAL2 expression, indicating a potential regulatory relationship between these proteins in pancreatic cancer cells. Consistent with this idea, HIF2A levels were increased in *BMAL2* knockout cells. In line with the blunted lactate increase seen in *BMAL2* knockout cells, we found LDHA protein levels, a key protein involved in the glycolytic process, to be significantly reduced in these cells under normoxic and even more in

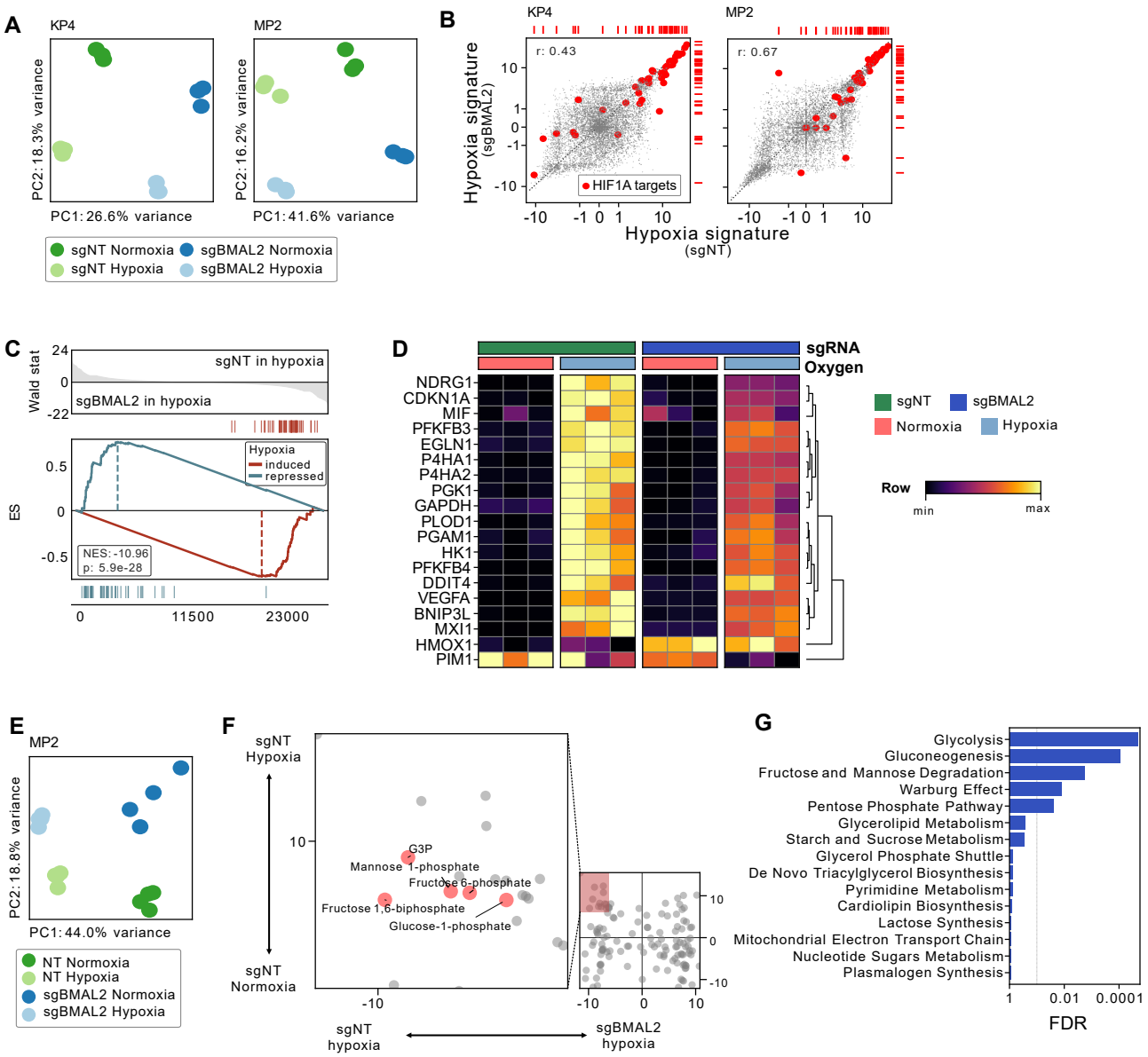

Figure 6: (**A**) Principal component analysis (PCA) based on gene expression of the indicated cell line carrying sgNT or sgBMAL2 in hypoxic or normoxic environments, respectively. (**B**) Scatter plot illustrating the relationship of a genome-wide transcriptional hypoxia signature found in the indicated cell lines carrying sgNT (x-axis) and sgBMAL2 (y-axis), respectively. Red circles mark a set of HIF1A reporter genes described previously (Ref. [48]) (**C**) 2-tailed GSEA of the top 100 transcripts induced (red) and repressed (blue) by hypoxia in PDAC cells on a gene expression signature between hypoxic sgBMAL2 cells (left) and sgNT cells (right). (**D**) Heatmap illustrating HIF1A reporter gene expression (Ref. [48]) for a subset with a differential hypoxia response between cells carrying sgNT and sgBMAL2, respectively. (**E**) PCA based on metabolite abundances in sgBMAL2 vs sgNT MP2 cells in hypoxic or normoxic environments, respectively. (**F**) Differential abundance signatures of 230 metabolites in MP2 in hypoxic cells carrying sgNT (left) vs. sgBMAL2 (right) (x-axis) and sgNT cells in hypoxic (top) vs. normoxic (bottom) conditions (y-axis). Zoomed area shows metabolites with opposite behavior and red circles mark members of the glycolysis/fructose metabolic pathways. (**G**) Overrepresentation analysis of the indicated metabolite sets among metabolites from the upper left quarter from (**F**).

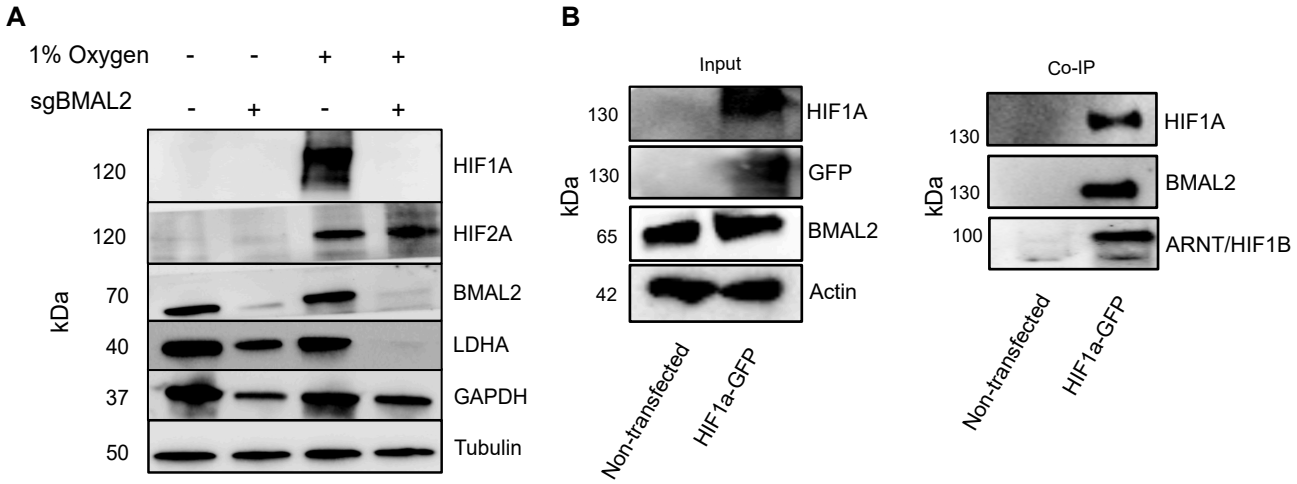

Figure 7: (**A**) Western Blot for HIF1A, HIF2A, BMAL2, LDHA and GAPDH in PANC1 cells carrying the indicated sgRNA in the indicated oxygen environment (24h). Tubulin was the loading control. (**B**) Input Control: Total cell lysates were subjected to Western blotting to verify the expression levels of HIF1A, GFP and BMAL2. Co-IP: Cell lysates were immunoprecipitated using anti-HIF1A, anti-BMAL2 and anti-ARNT (HIF1B) antibodies. The immunoprecipitated proteins were then analyzed by Western blotting.

hypoxic conditions (**Figure 7A**). Finally, to test whether a physical interaction with HIF1A could contribute to BMAL2's stabilizing function of the hypoxia response, we carried out Co-IP experiments using overexpression of HIF1A-GFP constructs (**Figure 7B**) showing a direct protein-protein interaction between BMAL2 and HIF1A. This interaction could have significant implications for the regulation of key cellular processes involved in pancreatic cancer progression.

Altogether, we find the PAS family member BMAL2 to operate downstream of mutant KRAS to implement key phenotypic transitions in pancreatic carcinogenesis. Its genetic perturbation in pancreatic cancer cells produces hypoxia-specific phenotypes by preventing HIF1A stabilization resulting in a blunted transcriptional and metabolic response to low oxygen environments.

Discussion

The conservation of genomic alterations between precursor lesions, primary and metastatic PDAC tumors [1, 2, 16] has centered our efforts to identify (non-genetic) regulatory drivers of PDAC malignancy. As expected, by carefully anchoring our expression profiles to meticulous histopathological annotation, we find that epithelial differentiation state is closely mirrored by transcriptional regulatory programs. However, the availability of profiles from benign precursors contextualizes our observations of malignant samples. For example, oncogenic properties have frequently been ascribed to transcription factors, such as GATA6, that are "overexpressed" in the (well-differentiated) Classical subtype, relative to other PDAC tumors [15, 24]. However, GATA6 activity was significantly higher in benign precursors than in low-grade tumors. We infer that the comparatively high activity of GATA6 in low-grade tumors reflects an incomplete loss of differentiation state, consistent with functional characterizations [58, 59] that point to a largely tumor-suppressive role for GATA6. We find a similar pattern of downregulation in PDAC for the majority of pancreatic transcription factors, including PDX1, HNF1B, and SOX9, calling into question their role as "drivers" of low-grade, Classical tumors. As loss of differentiation in high-grade tumors is associated with worse prognosis [60, 61], we urge caution in attempts to target GI transcription factors therapeutically, at any stage of disease, and would instead favor strategies that target consistent RPs of multiple malignant phenotypes.

The *KRAS* oncogene plays a central role in the initiation and maintenance of pancreatic tumors and its signaling network represents a major target for therapeutic intervention [62–66]. However, while virtually all aspects of PDAC biology are influenced by mutations in *KRAS*, their association to histopathological and transcriptional phenotypes appears to be limited [67, 68]. On the contrary, copy number gains of the mutant *KRAS* allele, rather than specific single nucleotide variations were shown to parallel histological dedifferentiation [69] and were overrepresented in metastatic disease and the basal-like phenotype, respectively [15]. However, both phenomena occur also in the absence of increased KRAS gene dosage, suggesting that their implementation relies also on epigenetic and transcriptional mechanisms. Our results concerning KRAS activity, which can be inferred for individual tumors independent from genomic events by assessing the distribution of context-specific KRAS target genes, fit in well with these observations. For example, we find KRAS activity is lowest in low-grade precursor lesions, despite the high prevalence of activating *KRAS* mutations [1] in PanIN. With the progression to PDAC and eventual dedifferentiation to tumors of non-gland forming growth [70], KRAS activity increases steadily - a pattern that is best mirrored by the activity of the bHLH-PAS family member BMAL2. Our

pharmacologic perturbation data suggest that BMAL2, and by extension KRAS, activity is best reverted by inhibitors targeting downstream pathways at the level of MEK and ERK, placing BMAL2 functionally close to well-validated downstream effectors of the RAS-MEK-ERK cascade such as MYC [28, 71] and ETS1 [72] (the latter of which is a direct target of BMAL2 in our regulatory network).

Hypoxia, a state of low oxygen, is commonly linked to a poor prognosis in PDAC, promoting cancer cell proliferation, epithelial-to-mesenchymal transition (EMT), invasiveness, resistance to therapies and metastasis [73–76]. Transcriptional responses to hypoxia are canonically mediated by the oxygen-regulated hypoxia-inducible factors HIF1A and HIF2A, which bind as heterodimers to HIF1B. Though similar in structure, the HIF alpha proteins drive divergent responses to hypoxia, with HIF1A promoting the more classic hypoxia responses such as glycolysis, whereas HIF2A is more associated with heme metabolism [77–81]. The possibility that BMAL2 can serve as a functional switch between HIF1A- and HIF2A-dependent hypoxic responses provides one potential answer to the long-standing question of how these proteins are differentially regulated. Certainly, a connection between RAS signaling and glycolysis has long been apparent [28, 82, 83], but our findings provide a novel mechanistic understanding of the relationship between RAS and hypoxic metabolism.

Our findings add to a growing body of evidence that circadian rhythm genes contribute to oncogenic processes, through a range of potential mechanisms including dysregulation of CLOCK and modulation of matrix metalloproteinase secretion [84, 85]. At least in the context of PDAC, BMAL2 appears to be most strongly associated with the fine regulation of hypoxic metabolism in response to RAS signaling. This result directly links the KRAS-dependent paracrine suppression of angiogenesis in PDAC [86] to a cell-autonomous regulatory program that enables survival in the results hypoxic microenvironment. As HIF-targeted drugs enter clinical development [87], our data not only deepen our understanding of the regulatory networks operating in pancreatic cancer cells, they also highlight a potential avenue for the therapeutic targeting of hypoxic metabolism. Further exploration of BMAL2 and other bHLH-PAS proteins and their impact on pancreatic cancer biology are warranted, with the ultimate goal of translating these insights into innovative treatment strategies for this challenging disease.

Data Availability Statement

The data generated in this study are available upon request from the corresponding author.

Ethics Statement

All mouse studies performed were approved by the Columbia University Irving Medical Center (CUIMC) Institutional Animal Care and Use Committee (IACUC). All work using patient samples was performed with approval from the CUIMC Institutional Review Board (IRB).

Acknowledgments

K.P.O and C.A.L were supported by the NCI (R01CA215607, R01CA244931). K.P.O was also supported by a Career Development Award from the Pancreatic Cancer Action Network and a Clinical Translational Research Award from the Lustgarten Foundation for Pancreatic Cancer Research. A.C.G received support from the Charles H. Revson Senior Postdoctoral Fellowship in Biomedical Science (Grant No. 22-22). K.J received research supported by New Hampshire- INBRE through an Institutional Development Award (IDeA), P20GM103506, from the National Institute of General Medical Sciences of the NIH. H.C.M received support from a Mildred Scheel Postdoctoral Fellowship (Deutsche Krebshilfe) and the KKF Clinician-Scientist program (TUM). This work utilized resources from the CU-DLDRC (P30 DK132710) and the Columbia University CCSG (5P30CA013696), including the Genomics, OPTIC, Database, and Molecular Pathology Shared Resources.

Author's contributions

H.C.M. and K.P.O conceived the project. H.C.M. started the project and performed the LCM dataset and the computational analyses. A.C.G. designed, performed and oversaw the experimental analyses and contributed to the computational analyses. S.H., C.C., C.F.P, S.A.S, A.A., L.Z., T.L., I.S., D.R.R., K.S., and J.G. contributed to experimental execution, data acquisition and data generation. G.A.M. and W.W. aided in the curation of human outcomes data. A.I. reviewed histopathology for pancreatic specimen used in the CUMC cohort. H.C.M, A.C.G., M.A.B and K.P.O. wrote the manuscript with feedback and editing from R.M.S., K.J., C.A.L, Y.S and A.C

Methods

Patient population and samples generation

Patient population. Freshly frozen tissue samples were obtained from patients who underwent surgical resection at the Pancreas Center at Columbia University Medical Center as described previously [9].

The clinical data of these patients are shown in Supplementary Tables S1 and S2. Before surgery, all patients had given surgical informed consent, which was approved by the institutional review board. Immediately after surgical removal, the specimens were cryopreserved, sectioned, and microscopically evaluated by the Columbia University Tumor Bank (IRB AAAB2667). Suitable samples were transferred into OCT medium (Tissue Tek) and snap-frozen in a 2-methylbutane dry ice slurry. The tissue blocks were stored at -80°C until further processing. H&E stained sections of frozen PDAC samples from the Tumor Bank were initially screened to confirm the diagnosis and overall sample RNA quality was assessed by the Pancreas Center supported Next Generation Tumor Banking program using gel electrophoresis, with samples exhibiting high RNA quality utilized for subsequent analyses.

Laser Capture Microdissection (LCM), RNA sequencing, and gene expression quantification. LCM-RNA-Seq was performed as described previously [9, 88]. Briefly, Cryosections of OCT-embedded tissue blocks were transferred to PEN membrane glass slides and stained with cresyl violet acetate. Adjacent sections were H&E stained for pathology review. Laser capture microdissection was performed on a PALM MicroBeam microscope (Zeiss), collecting at least 1000 cells per compartment. RNA was extracted and libraries were prepared using the Ovation RNA-Seq System V2 kit (NuGEN). Libraries were sequenced to a depth of 30million, 100bp, single-end reads on an Illumina HiSeq 2000 or 4000, respectively, platform. Reads and transcripts per million (TPM) were estimated for each transcript using the transcript sequences from the GENCODE Release 34 (GRCh38.p5) and the Salmon software (v1.3.0). Counts and TPM were summarized at the gene level by summing up the transcript values for each corresponding gene.

Computational methods

Assembly of a PDAC regulatory model and network analysis. A cell regulatory network for pancreatic carcinogenesis (CUMC-E interactome) was reverse-engineered by ARACNe-AP [5] using 242 epithelial LCM-RNA-Seq gene expression profiles. Genes with detection rates at 10 counts below 25% in all of the examined conditions (PanIN, IPMN, and PDAC) were removed and the variance was stabilized by fitting the dispersion to a negative binomial distribution as implemented in the *DESeq2* R package [89]. ARACNe was run with standard settings (using data processing inequality (DPI), with 100 bootstrap iterations using human gene symbols mapping to a set of 1665 transcription factors and 1025 transcription cofactors as described by AnimalTFDB 3.0 [90]. For the signaling network, a set of 3370 signaling-pathway-related genes was considered which were annotated in the GO Biological Process database as GO:0007165—'signal transduction' and in the GO Cellular Component database as GO:0005622—'intracellular' or GO:0005886—'plasma membrane'. Thresholds for the tolerated DPI and mutual information P value were set to 0 and 10–8, respectively. Using the strategy outlined above, we also generated a stromal regulatory network leveraging a set of 159 stromal LCM gene expression profiles (124 PDAC, 19 PanIN, 12 IPMN). Cytoscape v3.7.1 [91] was used to illustrate subnetworks of relevant regulatory proteins. The CUMC-E interactome is available as R object from https://doi.org/10.6084/m9.figshare.13160078.v2.

Master Regulator Analysis and inference of virtual protein activity. The enrichment of each regulatory protein's regulon in the progression and dedifferentiation signature, respectively, was inferred by the MARINa algorithm as implemented in the msviper function from the *viper* R package [26, 27, 92]. Statistical significance was estimated by permuting the sample labels uniformly at random 1,000 times. For single-sample analysis including precursor and tumor samples, unsupervised gene expression signatures were computed by a z-score transformation of the variance-stabilized data. This was performed gene-by-gene, by first subtracting the mean expression level across all samples and then dividing by its standard deviation. Relative protein activity was then inferred for each sample with the VIPER algorithm. For a patient-based approach including the assessment of whether significant dysregulation of an individual regulatory protein occurs in a given tumor, single sample gene expression signatures were computed for each primary sample by subtracting the mean of all precursor samples (n = 45) and dividing by their standard deviation. RP activity was then inferred by VIPER analysis of each PDAC gene expression signature. P-values were estimated by the analytical approximation implemented in the aREA algorithm, which is virtually equivalent to estimations obtained by permuting the genes in the signature uniformly at random [27]. P-values were corrected to account for multiple hypothesis testing by the Benjamini-Hochberg method.

Gene set enrichment analysis and scoring. One-tail gene set enrichment analysis was implemented as described [93]. Two-tailed gene set enrichment analysis and enrichment of individual ARACNe regulons were carried out using analytic rank-based enrichment analysis (aREA) [27]. Functional annotation of ARACNe-derived regulons was carried out by testing the overrepresentation of HALLMARK gene sets (MSigDb v6.0) among all target genes of a given regulatory protein with the gene universe set to all unique genes in the CUMC-E interactome (n=18658) using a two-tailed Fisher's Exact test.

Differential gene expression. Genome-wide differential gene expression analysis was generally calculated using the *DESeq2* [89] R package for RNA-Seq count data and the *limma* R package [94] for microarray data. For comparisons including both RNA-Seq and microarray data, differential gene expression for count data was repeated using the voom-limma

framework for the sake of consistency with the microarray analysis.

Survival signature and assessment of prognostic relevance. In an unbiased approach to study the association of gene expression and protein activity with patient outcome, a genome-wide survival signature was computed by fitting a multivariate Cox Proportional Hazards model (CPHM) accounting for the age at diagnosis and the continuous, normalized expression of a respective gene using the *survival* R package [95]. Next, we extracted the ensuing Wald statistic of the coefficient for gene expression with higher values corresponding to higher hazard ratios and vice versa and applied MARINa with a gene permutation null model to this survival signature to infer regulatory proteins controlling the survival signature.

Effect size meta-analysis. The effect size (i.e. $\log_2$ fold change) and its standard error for BMAL2 were extracted from the respective genome-wide differential expression analysis of a total of 10 studies where global expression in normal vs. primary tumors and low-grade vs. high-grade tumors, respectively, was contrasted. Similarly, the coefficient (log hazard ratio) and its standard error for the upper tertile of BMAL2 expression and activity, respectively, were extracted from a CPHM in cohorts with available time-to-event data. Meta-analysis was carried out using the *metafor* R package [96]. Both random and fixed effect models were fit using the rma function (method = "REML" and method = "FE").

Molecular subtyping. Moffitt classes were determined for 197 primary PDAC LCM-RNA-Seq profiles as described previously [36]. Briefly, using the 50 (47 with a unique match in our data) tumor-specific transcripts from Moffitt et al., we applied consensus clustering to our mRNA cohort with Euclidean distance and the partitioning around medoids (PAM) algorithm, seeking and reproducing two clusters of both genes and samples.

PAS family sequence alignment. Amino acid sequences for bHLH-PAS family members were retrieved using functionality from the Universal Protein Resource Knowledgebase [97]. After sequence alignment pair-wise distances determined based on sequence identity. Results were illustrated using the *ggtree* and *msatools* R packages.

Hypoxia scoring. Using tumor epithelial expression data, hypoxia scores were calculated by using mRNA-based signatures as described previously [52]. For each gene in each of eight signatures, TPM were extracted and if a tumor's abundance value exceeded the median across all tumors, +1 was added to its hypoxia score while -1 was added otherwise.

External data

Human PDAC cohorts. For the TCGA-PAAD cohort, raw count data were retrieved from the GDC Data portal for 149 patients described previously [42] and the variance was stabilized as described above. For the ICGC-PACA-AU cohort described previously [44], normalized gene expression data for 96 patients were provided by the authors in Suppl. Table 2. Microarray data of primary PDAC specimen from Collisson et al. [24] (n = 27), Moffitt et al. [36] (n = 252), and Puleo et al. [43] (n = 309) were retrieved from GSE17891, GSE71729 and E-MTAB-6134, respectively. Studies containing expression data from both normal pancreas and PDAC were processed and analyzed as described previously [98].

TCGA Pan-Cancer Atlas. Processed clinical and expression data were retrieved from the Genomic Data Commons Pan-Cancer homepage (https://gdc.cancer.gov/about-data/publications/pancanatlas). Information on sample types was added using TCGA sample barcodes. For regulatory network assembly, only tumor types with at least 100 RNA-Seq samples were retained and networks were generated using ARACNe as described above for CUMC samples.

Gene perturbation signatures. Raw microarray data from a mouse model harboring a dox-inducible oncogenic *Kras*^{G12D} were retrieved from GSE32277 [28] and GSE58307 [29] and processed using the affy and gcrma R packages. Processed microarray data from normal murine ductal cells in which oncogenic *Kras*^{G12D} was turned on using adenoviral Cre recombinase were retrieved from GSE89846 and E-MTAB-2592 [30, 32]. Raw RNA-Seq data from human PDAC cell lines stably transfected with shRNA targeting KRAS were retrieved from the European Nucleotide Archive under accession PRJEB25797 [31] and quantified using the pipeline outlined above for CUMC samples. RNA-Seq counts were analyzed using the voom-limma framework implemented in the *edgeR* and *limma* R packages.

ChIP-Atlas. We identified ChIP-Seq experiments concerning transcription factors in a cellular context pertinent to pancreatic ductal adenocarcinoma via the ChIP-Atlas [21] website. The results of this search are listed in Supplementary Table S3. For each experiment and transcription factor, we tested whether ARACNe-inferred targets of the respective transcription factor were overrepresented among ChIP-Seq inferred targets using a Fisher's Exact test with subsequent adjustment of p-values using the Benjamini-Hochberg method.

Experimental methods

Cell culture. KP4, PANC1, MIAPACA2 (MP2), and PATU8902 cell lines were obtained from ATCC and tested negative for mycoplasma infection. Cells were maintained under standard conditions at 37ºC and 5% CO2 using manufactured cell media conditions.

Genome editing and transfection protocol. The sgRNA (small-guide RNA) for knocking out *BMAL2* as well as a non-targeting (NT) sequence were purchased from GenScript (Piscataway, NJ) using the pLentiGuide-Puro vector as a backbone. Human

PDAC cells were first infected with a pLentiCas9-Blast vector (Addgene, #52962) for a constitutive Cas9 expression and selected with Blasticidin (AG Scientific, #B-1247-SOL). Cells expressing Cas9 were then infected with selected virus carrying sgBMAL2 and sgNT, respectively, using the lentiviral protocol according to the manufacturer's instructions.

Viability, lactate and migration assays. Cells were seeded at $3x10^3$ cells per well in 96 well plates and incubated for five days either under normoxia or moved to the hypoxia chamber with 1% O_2 (StemCell, #27310). After the incubation time, lactate assay was performed using 5 µl of media and the luminometric Lactate-Glo assay kit (Promega, #J5021) according to the manufacturer's protocol. To measure cell viability, Alamar Blue reagent (Bio-rad, #BUF012) was added to the culture media for 4h, and absorbance was determined at 570 and 600 nm using a Varioskan LUX Multimode Microplate Reader (Thermo, #3020-80389). For the migration assay, PDAC cells carrying sgNT or sgBMAL2, respectively, were seeded ($1×10^5$) into transwell membrane inserts in serum-free culture media (5 µm pore, Corning #3412) and regular media was added to the lower chamber. Cells were incubated for 24h in regular conditions. After the incubation time, plates were incubated either under normoxia (37°C, 5% CO_2, 20% O_2) or moved to the hypoxia chamber (37°C, 5% CO_2, 1% O_2) for 14 hours and cells that migrated across the membrane were fixed and stained with crystal violet and counted under the microscope.

Immunoblotting. Cell pellets were lysed with RIPA lysis buffer (Cell Signaling, #9806S) and protein concentrations were determined by BCA protein assay (Thermo Scientific, #23227) according to the manufacture's protocol. Proteins were separated on Mini-PROTEAN TGX gels (Bio-Rad, #4561093) and transferred to nitrocellulose membrane (Bio-Rad, #1704156). Membranes were incubated in blocking buffer (5% BSA, 0.1% Tween-20, 10 mM Tris at pH 7.6, 100 mM NaCl) for 1 hour and then with primary antibody overnight at 4°C according to the antibody datasheet. Antibodies used: HIF1A (1:1000, Cell Signaling, #36169S), beta-Actin (1:1000, Cell Signaling, #4970S), HIF2A (1:1000, Cell Signaling, #7096S), BMAL2 (1:500, Abcam, #ab221557), LDHA (1:1000, Cell Signaling, #3582S), GAPDH (1:1000, Cell Signaling, #2118S) and Tubulin (1:1000, Cell Signaling, #2146S). Anti-rabbit-HRP (Cell Signaling, #7074S) conjugated antibody was used to detect the desired protein by chemoluminescence with ECL (Bio-Rad, #170-5061).

Metabolomics. Metabolites were extracted from cell pellets by adding 1mL of ice-cold 80% MeOH / 20% H_2O. Samples were vortexed and incubated on dry ice for 10 minutes, centrifuged at 12,000g, with subsequent extraction of the supernatant. Supernatant was volume normalized across sample groups and then concentrated using a SpeedVac Vacuum Concentrator (model: SPD1030), and reconstituted in 50µL of 50% MeOH / 50% H_2O. Samples were run on a tandem liquid-chromatography mass spectrometry (LC/MS) set up consisting of an Agilent 1290 Infinity II LC and Agilent 6470 Triple Quadrupole (QqQ) mass spectrometer. The method and column parameters were as follows: Solvent A: 97% water and 3% methanol 15 mM acetic acid and 10 mM tributylamine (pH of 5). Solvent C: 15 mM acetic acid and 10 mM tributylamine in methanol. Solvent D for washing is acetonitrile. LC system seal washing solvent: 90% water and 10% isopropanol. Needle wash solvent: 75% methanol and 25% water. GC-grade Tributylamine 99% (ACROS ORGANICS), LC/MS grade acetic acid Optima (Fisher Chemical), InfinityLab Deactivator additive, ESI–L Low concentration Tuning mix (Agilent Technologies), LC-MS grade solvents of water, and acetonitrile, methanol (Millipore), isopropanol (Fisher Chemical). Column: Agilent ZORBAX RRHD Extend-C18, 2.1 × 150 mm and a 1.8 µm and ZORBAX Extend Fast Guards for ultra high performance liquid chromatography (UHPLC). LC gradient profile: 0.25 mL/min, 0–2.5 min, 100% A; 7.5 min, 80% A and 20% C; 13 min 55% A and 45% C; 20 min, 1% A and 99% C; 24 min, 1% A and 99% C; 24.05 min, 1% A and 99% D; 27 min, 1% A and 99% D; at 0.8 mL/min, 27.5–31.35 min, 1% A and 99% D; at 0.6 mL/min, 31.50 min, 1% A and 99% D; at 0.4 mL/min, 32.25–39.9 min, 100% A; and at 0.25 mL/min, 40 min, 100% A. Column temperature was kept at 35°C, samples were at 4°C and the injection volume was 2 µL per sample.The 6470 Triple Quad MS is calibrated with the Agilent ESI-L Low concentration Tuning mix. Source parameters: gas temperature 150°C, gas flow 10 L/min, nebulizer 45 psi, sheath gas temperature 325°C, sheath gas flow 12 L/min, capillary –2000 V, and delta EMV –200 V. Negative ion mode was used. Dynamic multiple reaction monitoring (dMRM) scan type is used with 0.07 min peak width, acquisition time is 24 min. Delta retention time of plus and minus 1 min, fragmentor of 40 eV, and cell accelerator of 5 eV are incorporated in the method. Data were pre-processed with Agilent MassHunter Workstation Quantitative Analysis for QQQ version 10.1, build 10.1.733.0.

Co-immunoprecipitation. HEK cells were transfected 24 h after plating. Mixed homemade PEI 3µl with 1µg of plasmid in 200µls of Opti MEM per well of a 6 well plate, incubated at room temperature for 20mins, then gently added to the cells. Cells were lysed (6 wells of a 6 well plate combined) per condition with RIPA buffer supplemented with protease inhibitor cocktail, sodium orthovanadate, MgCl, DNaseI and EDTA (final concentration of all these at 1mM). Lysates were incubated on ice for 20mins, then spun down at 15,000rpm for 15mins, with subsequent collection of the supernatant. 90% of supernatant volume were incubated with GFP beads (already washed according to manufacturer's protocol) and the remaining 10% were used as input control. Incubation with GFP beads continued at 4°C for two hours while mixing. Afterwards, samples were washed three times according to manufacturer's protocol and then bead-bound protein was diluted with 2X dye and boiled at 95°C for

10mins.

RNA extraction and RNA sequencing. Total RNA from proliferation assays was extracted using TRIzol (Invitrogen) according to the manufacturer's protocol and the quality of the sample was analyzed using the 2100 bioanalyzer system (Agilent). Samples were then sequenced using the Element AVITI platform.

KPC Mice. *LSL-Kras*$^{G12D/+}$;*LSL-Trp53*$^{R172H/+}$;*Pdx1-Cre* (KPC) mice were bred by crossing the *LSL-Kras*$^{G12D/+}$, *LSL-Trp53*$^{R172H/+}$ and *Pdx1-Cre* strains. Triple mutant mice were palpated twice weekly for evidence of early tumors beginning at 8 weeks of age, followed by subsequent B-mode ultrasound screening using a VisualSonics 2100 Vevo High Resolution System. Following detection, tumors were monitored once weekly until reaching a mean diameter of 6 mm.

Oxylite Measurements. Intratumoral partial oxygen pressures in KPC mice (n=16) were measured using the Oxylite fluorescence quenching-based system (Oxford Optronics). Tumor-bearing KPC mice were anesthetized with 2% isoflurane in either air or pure oxygen. Hair was removed with depilatory cream around the abdomen and the tumor was visualized by ultrasound. A syringe with a 21G needle was attached to a stereotactic mount and inserted through the skin and abdominal wall. Real-time ultrasound imaging was used to visually guide the needle in-plane with the image through the center of the tumor until reaching the far edge. With the needle in place, the syringe was carefully removed and the bare-fiber oxygen-sensing OxyliteTM probe was then attached to the stereotactic mount and threaded through the needle bore until the probe tip was localized at the far edge of the tumor. The needle was fully retracted over the fiber and an initial pO2 measurement was taken at the far site. Prior to each measurement, the probe was allowed to equilibrate for 3-5 minutes until readings stabilized. After the initial reading, the fiber was retracted incrementally through the needle track, with readings taken every 1-2 mm, through the full depth of the tumor (ranged from 6-12 mm in diameter). Measurements within 1 mm of the edge of the tumor were excluded from the analysis since the needle frequently punctured the far wall of the tumor, allowing oxygen from the abdominal cavity into the wound (as made apparent by a sharp spike in readings). To compare tumor to normal tissue, partial pressures were also measured in pancreas and kidney of WT mice (n=4) kept under anesthesia using compressed air as vehicle. After completing measurements, mice were euthanized by isoflurane overdose and tissue was harvested for formalin fixation for 24 h prior to paraffin embedding. All tumors were verified as pancreatic ductal adenocarcinoma by a blinded observer experienced in mouse tumor pathology.

References

1. Murphy, S. J. *et al.* Genetic alterations associated with progression from pancreatic intraepithelial neoplasia to invasive pancreatic tumor. *Gastroenterology* **145,** 1098–1109.e1 (2013).
2. Makohon-Moore, A. P. *et al.* Limited heterogeneity of known driver gene mutations among the metastases of individual patients with pancreatic cancer. *Nat. Genet.* **49,** 358–366 (2017).
3. Califano, A. & Alvarez, M. J. The recurrent architecture of tumour initiation, progression and drug sensitivity. *Nat. Rev. Cancer* **17,** 116–130 (2017).
4. Basso, K. *et al.* Reverse engineering of regulatory networks in human B cells. *Nat. Genet.* **37,** 382–390 (2005).
5. Lachmann, A., Giorgi, F. M., Lopez, G. & Califano, A. ARACNe-AP: gene network reverse engineering through adaptive partitioning inference of mutual information. *Bioinformatics* **32,** 2233–2235 (2016).
6. Aytes, A. *et al.* Cross-species regulatory network analysis identifies a synergistic interaction between FOXM1 and CENPF that drives prostate cancer malignancy. *Cancer Cell* **25,** 638–651 (2014).
7. Piovan, E. *et al.* Direct reversal of glucocorticoid resistance by AKT inhibition in acute lymphoblastic leukemia. *Cancer Cell* **24,** 766–776 (2013).
8. Carro, M. S. *et al.* The transcriptional network for mesenchymal transformation of brain tumours. *Nature* **463,** 318–325 (2010).
9. Maurer, C. *et al.* Experimental microdissection enables functional harmonisation of pancreatic cancer subtypes. *Gut* **68,** 1034–1043 (2019).
10. Basturk, O. *et al.* A Revised Classification System and Recommendations From the Baltimore Consensus Meeting for Neoplastic Precursor Lesions in the Pancreas. *Am. J. Surg. Pathol.* **39,** 1730–1741 (2015).
11. Maitra, A. & Leach, S. D. Disputed paternity: the uncertain ancestry of pancreatic ductal neoplasia. *Cancer Cell* **22,** 701–703 (2012).
12. Patra, K. C., Bardeesy, N. & Mizukami, Y. Diversity of Precursor Lesions For Pancreatic Cancer: The Genetics and Biology of Intraductal Papillary Mucinous Neoplasm. *Clin. Transl. Gastroenterol.* **8,** e86 (2017).
13. Matthaei, H. *et al.* Presence of pancreatic intraepithelial neoplasia in the pancreatic transection margin does not influence outcome in patients with R0 resected pancreatic cancer. *Ann. Surg. Oncol.* **18,** 3493–3499 (2011).
14. Mueller, S. *et al.* Evolutionary routes and KRAS dosage define pancreatic cancer phenotypes. *Nature* **554,** 62–68 (2018).
15. Chan-Seng-Yue, M. *et al.* Transcription phenotypes of pancreatic cancer are driven by genomic events during tumor evolution. *Nat. Genet.* **52,** 231–240 (2020).

16. Connor, A. A. *et al.* Integration of Genomic and Transcriptional Features in Pancreatic Cancer Reveals Increased Cell Cycle Progression in Metastases. *Cancer Cell* **35,** 267–282.e7 (2019).

17. Somerville, T. D. D. *et al.* TP63-Mediated Enhancer Reprogramming Drives the Squamous Subtype of Pancreatic Ductal Adenocarcinoma. *Cell Rep.* **25,** 1741–1755.e7 (2018).

18. Hayashi, A. *et al.* A unifying paradigm for transcriptional heterogeneity and squamous features in pancreatic ductal adenocarcinoma. *Nature Cancer* **1,** 59–74 (2020).

19. Compagno, M. *et al.* Mutations of multiple genes cause deregulation of NF-kappaB in diffuse large B-cell lymphoma. *Nature* **459,** 717–721 (2009).

20. Elyada, E. *et al.* Cross-Species Single-Cell Analysis of Pancreatic Ductal Adenocarcinoma Reveals Antigen-Presenting Cancer-Associated Fibroblasts. *Cancer Discov.* **9,** 1102–1123 (2019).

21. Oki, S. *et al.* ChIP-Atlas: a data-mining suite powered by full integration of public ChIP-seq data. *EMBO Rep.* **19** (2018).

22. Roe, J.-S. *et al.* Enhancer Reprogramming Promotes Pancreatic Cancer Metastasis. *Cell* **170,** 875–888.e20 (2017).

23. Wang, L. *et al.* Oncogenic function of ATDC in pancreatic cancer through Wnt pathway activation and beta-catenin stabilization. *Cancer Cell* **15,** 207–219 (2009).

24. Collisson, E. A. *et al.* Subtypes of pancreatic ductal adenocarcinoma and their differing responses to therapy. *Nat. Med.* **17,** 500–503 (2011).

25. Somerville, T. D. D. *et al.* ZBED2 is an antagonist of interferon regulatory factor 1 and modifies cell identity in pancreatic cancer. *Proc. Natl. Acad. Sci. U. S. A.* (2020).

26. Lefebvre, C. *et al.* A human B-cell interactome identifies MYB and FOXM1 as master regulators of proliferation in germinal centers. *Mol. Syst. Biol.* **6,** 377 (2010).

27. Alvarez, M. J. *et al.* Functional characterization of somatic mutations in cancer using network-based inference of protein activity. *Nat. Genet.* **48,** 838–847 (2016).

28. Ying, H. *et al.* Oncogenic Kras maintains pancreatic tumors through regulation of anabolic glucose metabolism. *Cell* **149,** 656–670 (2012).

29. Viale, A. *et al.* Oncogene ablation-resistant pancreatic cancer cells depend on mitochondrial function. *Nature* **514,** 628–632 (2014).

30. Sivakumar, S., de Santiago, I., Chlon, L. & Markowetz, F. Master Regulators of Oncogenic KRAS Response in Pancreatic Cancer: An Integrative Network Biology Analysis. *PLoS Med.* **14,** e1002223 (2017).

31. Bryant, K. L. *et al.* Combination of ERK and autophagy inhibition as a treatment approach for pancreatic cancer. *Nat. Med.* **25,** 628–640 (2019).

32. Diersch, S. *et al.* Kras(G12D) induces EGFR-MYC cross signaling in murine primary pancreatic ductal epithelial cells. *Oncogene* **35,** 3880–6 (2016).

33. Alvarez, M. J. *et al.* A precision oncology approach to the pharmacological targeting of mechanistic dependencies in neuroendocrine tumors. *Nat. Genet.* **50,** 979–989 (2018).

34. Mundi, P. S. *et al.* A Transcriptome-Based Precision Oncology Platform for Patient-Therapy Alignment in a Diverse Set of Treatment-Resistant Malignancies. *Cancer Discov* **13,** 1386–1407 (2023).

35. Kirby, M. K. *et al.* RNA sequencing of pancreatic adenocarcinoma tumors yields novel expression patterns associated with long-term survival and reveals a role for ANGPTL4. *Mol. Oncol.* **10,** 1169–1182 (2016).

36. Moffitt, R. A. *et al.* Virtual microdissection identifies distinct tumor- and stroma-specific subtypes of pancreatic ductal adenocarcinoma. *Nat. Genet.* **47,** 1168–1178 (2015).

37. Pilarsky, C. *et al.* Activation of Wnt signalling in stroma from pancreatic cancer identified by gene expression profiling. *J. Cell. Mol. Med.* **12,** 2823–2835 (2008).

38. Pei, H. *et al.* FKBP51 affects cancer cell response to chemotherapy by negatively regulating Akt. *Cancer Cell* **16,** 259–266 (2009).

39. Yang, S. *et al.* A Novel MIF Signaling Pathway Drives the Malignant Character of Pancreatic Cancer by Targeting NR3C2. *Cancer Res.* **76,** 3838–3850 (2016).

40. Hiraoka, N. *et al.* CXCL17 and ICAM2 are associated with a potential anti-tumor immune response in early intraepithelial stages of human pancreatic carcinogenesis. *Gastroenterology* **140,** 310–321 (2011).

41. Donahue, T. R. *et al.* Integrative survival-based molecular profiling of human pancreatic cancer. *Clin. Cancer Res.* **18,** 1352–1363 (2012).

42. Cancer Genome Atlas Research Network. Electronic address, a. a. d. h. e. & Cancer Genome Atlas Research, N. Integrated Genomic Characterization of Pancreatic Ductal Adenocarcinoma. *Cancer Cell* **32,** 185–203.e13 (2017).

43. Puleo, F. *et al.* Stratification of Pancreatic Ductal Adenocarcinomas Based on Tumor and Microenvironment Features. *Gastroenterology* **155,** 1999–2013.e3 (2018).

44. Bailey, P. *et al.* Genomic analyses identify molecular subtypes of pancreatic cancer. *Nature* **531,** 47–52 (2016).

45. The, G. C. The Genotype-Tissue Expression (GTEx) pilot analysis: Multitissue gene regulation in humans. *Science* **348,** 648–660 (2015).

46. Hoadley, K. A. *et al.* Cell-of-Origin Patterns Dominate the Molecular Classification of 10,000 Tumors from 33 Types of Cancer. *Cell* **173,** 291–304.e6 (2018).

47. Ghandi, M. *et al.* Next-generation characterization of the Cancer Cell Line Encyclopedia. *Nature* **569,** 503–508 (2019).

48. Li, B. *et al.* Fructose-1,6-bisphosphatase opposes renal carcinoma progression. *Nature* **513,** 251–5 (2014).

49. Labrecque, M. P., Prefontaine, G. G. & Beischlag, T. V. The aryl hydrocarbon receptor nuclear translocator (ARNT) family of proteins: transcriptional modifiers with multi-functional protein interfaces. *Curr. Mol. Med.* **13,** 1047–1065 (2013).

50. Hogenesch, J. B. *et al.* The basic helix-loop-helix-PAS protein MOP9 is a brain-specific heterodimeric partner of circadian and hypoxia factors. *J Neurosci* **20,** Rc83 (2000).

51. Maemura, K. *et al.* CLIF, a novel cycle-like factor, regulates the circadian oscillation of plasminogen activator inhibitor-1 gene expression. *J Biol Chem* **275,** 36847–51 (2000).

52. Bhandari, V. *et al.* Molecular landmarks of tumor hypoxia across cancer types. *Nat Genet* **51,** 308–318 (2019).

53. Olive, K. P. *et al.* Inhibition of Hedgehog signaling enhances delivery of chemotherapy in a mouse model of pancreatic cancer. *Science* **324,** 1457–61 (2009).

54. Koong, A. C. *et al.* Pancreatic tumors show high levels of hypoxia. *International Journal of Radiation Oncology*Biology*Physics* **48,** 919–922 (2000).

55. Vaupel, P., Thews, O. & Kelleher, D. K. Pancreatic tumors show high levels of hypoxia: regarding Koong et al. IJROBP 2000;48:919-922. *Int J Radiat Oncol Biol Phys* **50,** 1099–100 (2001).

56. Varghese, A. J., Gulyas, S. & Mohindra, J. K. Hypoxia-dependent Reduction of 1-(2-Nitro-1-imidazolyl)-3-methoxy-2-propanol by Chinese Hamster Ovary Cells and KHT Tumor Cells in Vitro and in Vivo1. *Cancer Research* **36,** 3761–3765 (1976).

57. Nakayama, K. & Kataoka, N. Regulation of Gene Expression under Hypoxic Conditions. *Int J Mol Sci* **20** (2019).

58. Martinelli, P. *et al.* GATA6 regulates EMT and tumour dissemination, and is a marker of response to adjuvant chemotherapy in pancreatic cancer. *Gut* **66,** 1665–1676 (2017).

59. Martinelli, P. *et al.* The acinar regulator Gata6 suppresses KrasG12V-driven pancreatic tumorigenesis in mice. *Gut* **65,** 476–486 (2016).

60. De Andrés, M. P. *et al.* GATA4 and GATA6 loss-of-expression is associated with extinction of the classical programme and poor outcome in pancreatic ductal adenocarcinoma. *Gut* **72,** 535–548 (2023).

61. Roy, N. *et al.* PDX1 dynamically regulates pancreatic ductal adenocarcinoma initiation and maintenance. *Genes Dev.* **30,** 2669–2683 (2016).

62. Collins, M. A. *et al.* Oncogenic Kras is required for both the initiation and maintenance of pancreatic cancer in mice. *J Clin Invest* **122,** 639–53 (2012).

63. Kemp, S. B. *et al.* Efficacy of a Small-Molecule Inhibitor of KrasG12D in Immunocompetent Models of Pancreatic Cancer. *Cancer Discov* **13,** 298–311 (2023).

64. Wasko, U. N. *et al.* Tumour-selective activity of RAS-GTP inhibition in pancreatic cancer. *Nature* **629,** 927–936 (2024).

65. Waters, A. M. & Der, C. J. KRAS: The Critical Driver and Therapeutic Target for Pancreatic Cancer. *Cold Spring Harb Perspect Med* **8** (2018).

66. Luo, J. KRAS mutation in pancreatic cancer. *Semin Oncol* **48,** 10–18 (2021).

67. Collisson, E. A., Bailey, P., Chang, D. K. & Biankin, A. V. Molecular subtypes of pancreatic cancer. *Nat. Rev. Gastroenterol. Hepatol.* **16,** 207–220 (2019).

68. Connor, A. A. & Gallinger, S. Pancreatic cancer evolution and heterogeneity: integrating omics and clinical data. *Nat Rev Cancer* **22,** 131–142 (2022).

69. Krasinskas, A. M., Moser, A. J., Saka, B., Adsay, N. V. & Chiosea, S. I. KRAS mutant allele-specific imbalance is associated with worse prognosis in pancreatic cancer and progression to undifferentiated carcinoma of the pancreas. *Mod Pathol* **26,** 1346–54 (2013).

70. S, N. K. *et al.* Morphological classification of pancreatic ductal adenocarcinoma that predicts molecular subtypes and correlates with clinical outcome. *Gut* **69,** 317–328 (2020).

71. Hayes, T. K. *et al.* Long-Term ERK Inhibition in KRAS-Mutant Pancreatic Cancer Is Associated with MYC Degradation and Senescence-like Growth Suppression. *Cancer Cell* **29,** 75–89 (2016).

72. Plotnik, J. P., Budka, J. A., Ferris, M. W. & Hollenhorst, P. C. ETS1 is a genome-wide effector of RAS/ERK signaling in epithelial cells. *Nucleic Acids Res* **42,** 11928–40 (2014).

73. Hoffmann, A. C. *et al.* High expression of HIF1a is a predictor of clinical outcome in patients with pancreatic ductal adenocarcinomas and correlated to PDGFA, VEGF, and bFGF. *Neoplasia* **10,** 674–9 (2008).

74. Miyake, K. *et al.* Expression of hypoxia-inducible factor-1alpha, histone deacetylase 1, and metastasis-associated protein 1 in pancreatic carcinoma: correlation with poor prognosis with possible regulation. *Pancreas* **36,** e1–9 (2008).

75. Sun, H. C. *et al.* Expression of hypoxia-inducible factor-1 alpha and associated proteins in pancreatic ductal adenocarcinoma and their impact on prognosis. *Int J Oncol* **30,** 1359–67 (2007).

76. Yokoi, K. & Fidler, I. J. Hypoxia increases resistance of human pancreatic cancer cells to apoptosis induced by gemcitabine. *Clin Cancer Res* **10,** 2299–306 (2004).

77. Chen, J. *et al.* Dominant-negative hypoxia-inducible factor-1 alpha reduces tumorigenicity of pancreatic cancer cells through the suppression of glucose metabolism. *Am J Pathol* **162,** 1283–91 (2003).

78. Chen, C. & Yu, Z. siRNA targeting HIF-1alpha induces apoptosis of pancreatic cancer cells through NF-kappaB-independent and -dependent pathways under hypoxic conditions. *Anticancer Res* **29,** 1367–72 (2009).

79. Wang, G. L., Jiang, B. H., Rue, E. A. & Semenza, G. L. Hypoxia-inducible factor 1 is a basic-helix-loop-helix-PAS heterodimer regulated by cellular O2 tension. *Proc Natl Acad Sci U S A* **92,** 5510–4 (1995).

80. Tian, H., McKnight, S. L. & Russell, D. W. Endothelial PAS domain protein 1 (EPAS1), a transcription factor selectively expressed in endothelial cells. *Genes Dev* **11,** 72–82 (1997).

81. Singhal, R. *et al.* HIF-2α activation potentiates oxidative cell death in colorectal cancers by increasing cellular iron. *J Clin Invest* **131** (2021).

82. Bryant, K. L., Mancias, J. D., Kimmelman, A. C. & Der, C. J. KRAS: feeding pancreatic cancer proliferation. *Trends Biochem Sci* **39,** 91–100 (2014).

83. Gaglio, D. *et al.* Oncogenic K-Ras decouples glucose and glutamine metabolism to support cancer cell growth. *Mol Syst Biol* **7,** 523 (2011).

84. Brady, J. J. *et al.* An Arntl2-Driven Secretome Enables Lung Adenocarcinoma Metastatic Self-Sufficiency. *Cancer Cell* **29,** 697–710 (2016).

85. Shafi, A. A. & Knudsen, K. E. Cancer and the Circadian Clock. *Cancer Res* **79,** 3806–3814 (2019).

86. Hasselluhn, M. C. *et al.* Tumor Explants Elucidate a Cascade of Paracrine SHH, WNT, and VEGF Signals Driving Pancreatic Cancer Angiosuppression. *Cancer Discov* (2023).

87. Yuan, X., Ruan, W., Bobrow, B., Carmeliet, P. & Eltzschig, H. K. Targeting hypoxia-inducible factors: therapeutic opportunities and challenges. *Nat Rev Drug Discov* **23,** 175–200 (2024).

88. Maurer, H. C. & Olive, K. P. Laser Capture Microdissection on Frozen Sections for Extraction of High-Quality Nucleic Acids. *Methods Mol. Biol.* **1882,** 253–259 (2019).

89. Love, M. I., Huber, W. & Anders, S. Moderated estimation of fold change and dispersion for RNA-seq data with DESeq2. *Genome Biol.* **15,** 550 (2014).

90. Hu, H. *et al.* AnimalTFDB 3.0: a comprehensive resource for annotation and prediction of animal transcription factors. *Nucleic Acids Res.* **47,** D33–D38 (2019).

91. Shannon, P. *et al.* Cytoscape: a software environment for integrated models of biomolecular interaction networks. *Genome Res.* **13,** 2498–2504 (2003).

92. Alvarez, M. J., Giorgi, F. & Califano, A. Using viper, a package for Virtual Inference of Proteinactivity by Enriched Regulon analysis. *Bioconductor,* 1–14 (2014).

93. Subramanian, A. *et al.* Gene set enrichment analysis: a knowledge-based approach for interpreting genome-wide expression profiles. *Proc. Natl. Acad. Sci. U. S. A.* **102,** 15545–15550 (2005).

94. Ritchie, M. E. *et al.* limma powers differential expression analyses for RNA-sequencing and microarray studies. *Nucleic Acids Res.* **43,** e47 (2015).

95. Therneau, T. M. & Grambsch, P. M. *Modeling Survival Data: Extending the Cox Model* 350 (Springer Science Business Media, 2013).

96. Viechtbauer, W. Conducting Meta-Analyses in R with the metafor Package. *Journal of Statistical Software, Articles* **36,** 1–48 (2010).

97. Zaru, R. & Orchard, S. UniProt Tools: BLAST, Align, Peptide Search, and ID Mapping. *Curr Protoc* **3,** e697 (2023).

98. Badgley, M. A. *et al.* Cysteine depletion induces pancreatic tumor ferroptosis in mice. *Science* **368,** 85–89 (2020).

Supplementary Figure 1

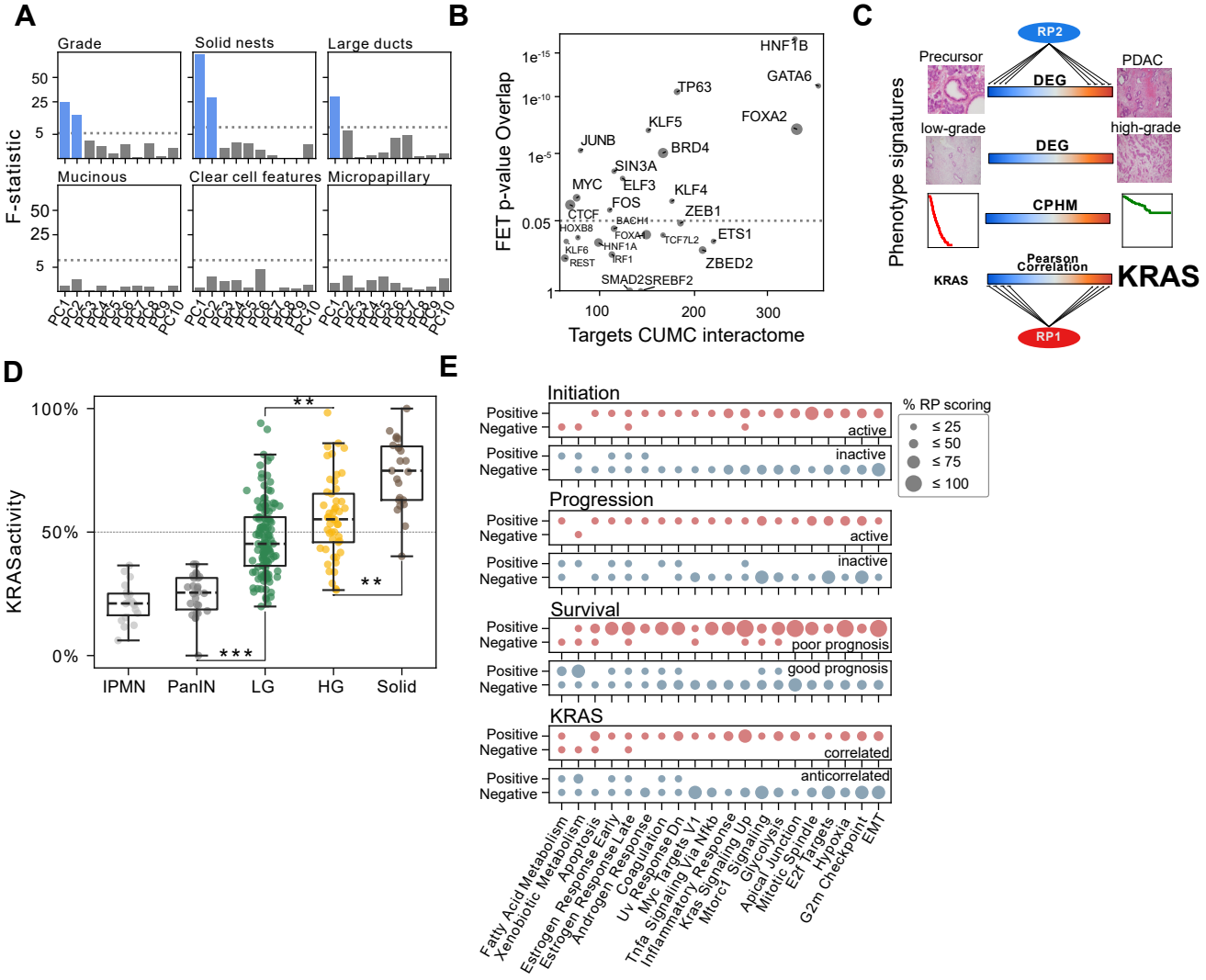

Supplementary Figure 1. (**A**) F-statistics (y-axis) from a linear model with the indicated principal component (PC, x-axis) as dependent variable and the indicated histopathological characteristic as the independent variable. Blue bars indicate significant results. (**B**) Scatter plot illustrating the relationship between number of ARACNe-inferred, context-specific targets for select regulatory proteins (RP, x-axis) and the significance of their overlap with targets deduced from publically available ChIP experiments as assessed by a two-tailed Fisher's Exact test. Circle size represents the number of publically available ChIP experiments (range = 1-4) (**C**) Schematic illustrating the assessment of regulatory protein activity in various genome-wide phenotype signatures. (**D**) KRAS protein activity across the indicated histological PDAC stages. Pairwise p-values are derived from a post hoc Dunn test after Kruskal-Wallis one-way analysis of variance (**E**) For each of 4 phenotypic signatures, regulons from the top 20 RP up (red color) and down (blue color) were divided into positive and negative targets (y-axis) which were then scored for overlap with the indicated HALLMARK gene sets (x-axis). Circle size represents the fraction of RPs (20 each) whose positive and negative regulon tail, respectively, exhibits significant overlap as assessed by a two-tailed Fisher's Exact test. **: $p \leq 0.01$, ***: $p \leq 0.001$

In boxplots, the box ranges from Q1 (the first quartile) to Q3 (the third quartile) of the distribution and the range represents the IQR (interquartile range). The median is indicated by a dashed line across the box. The “whiskers” on box plots extend from Q1 and Q3 to 1.5 times the IQR.

Supplementary Figure 2

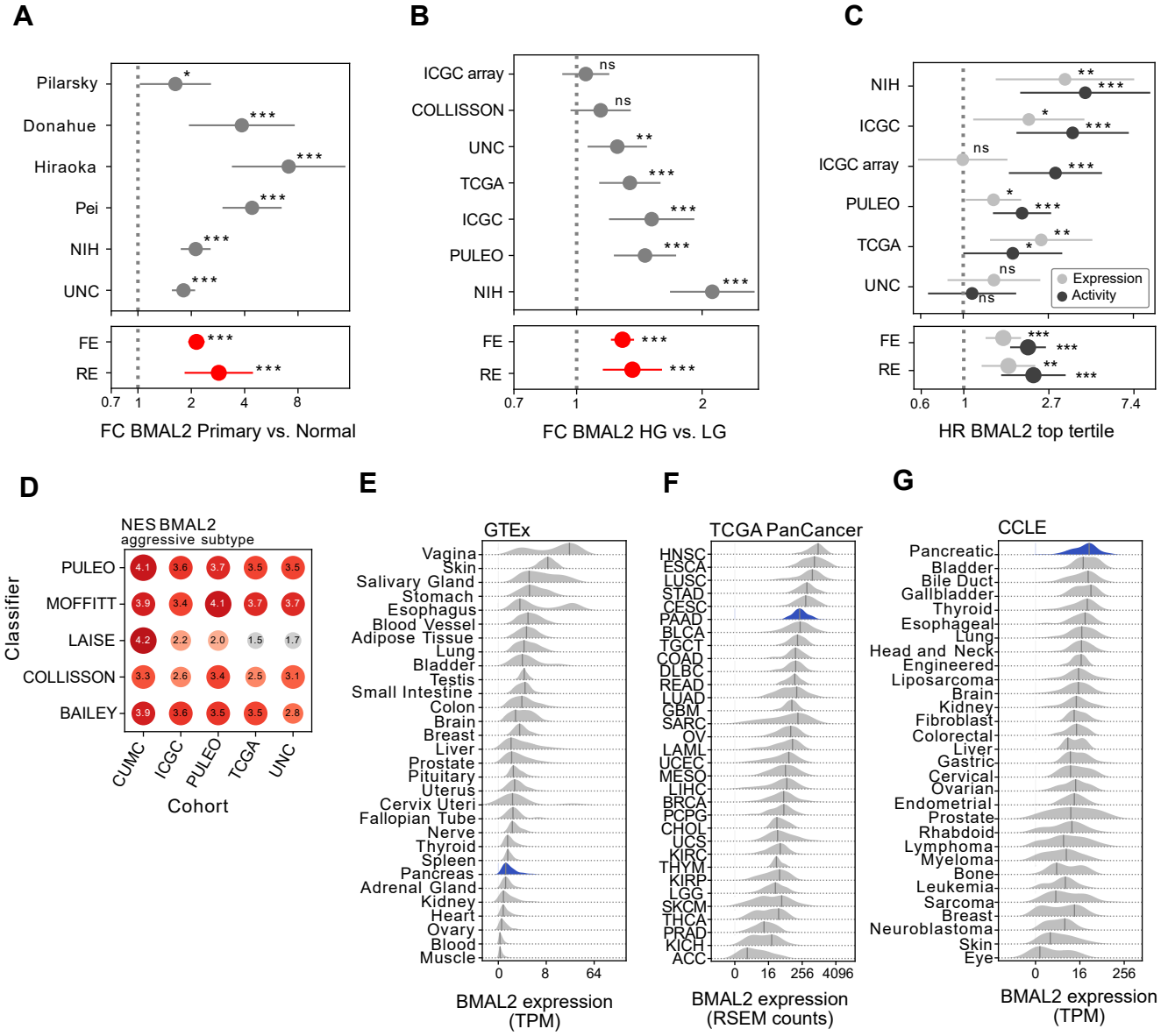

Supplementary Figure 2. Fold changes and their 95% confidence interval between (**A**) primary tumors and adjacent normal tissue, and (**B**) high-grade and low-grade tumors for the indicated data sets (y-axis). (**C**) Hazard ratios and their 95% confidence interval for patients belonging to the highest BMAL2 activity and expression tertile, respectively. Lower panels in (**A-C**) summarize the meta-analytic estimate from a fixed (FE) and random effects (RE) model, respectively. (**D**) BMAL2 activity (Normalized Enrichment Score, NES) in the most aggressive vs. least aggressive subtype as determined by the indicated classification scheme (y-axis) in each of the indicated data sets (x-axis). BMAL2 expression in the indicated units across (**E**) various normal tissues, (**F**) 33 primary tumor cohorts profiled by the TCGA Pan-Cancer project, and (**G**) cancer cell lines derived from various lineages profiled by the CCLE project. *: $p \leq 0.05$ **: $p \leq 0.01$, ***: $p \leq 0.001$, ns: not significant

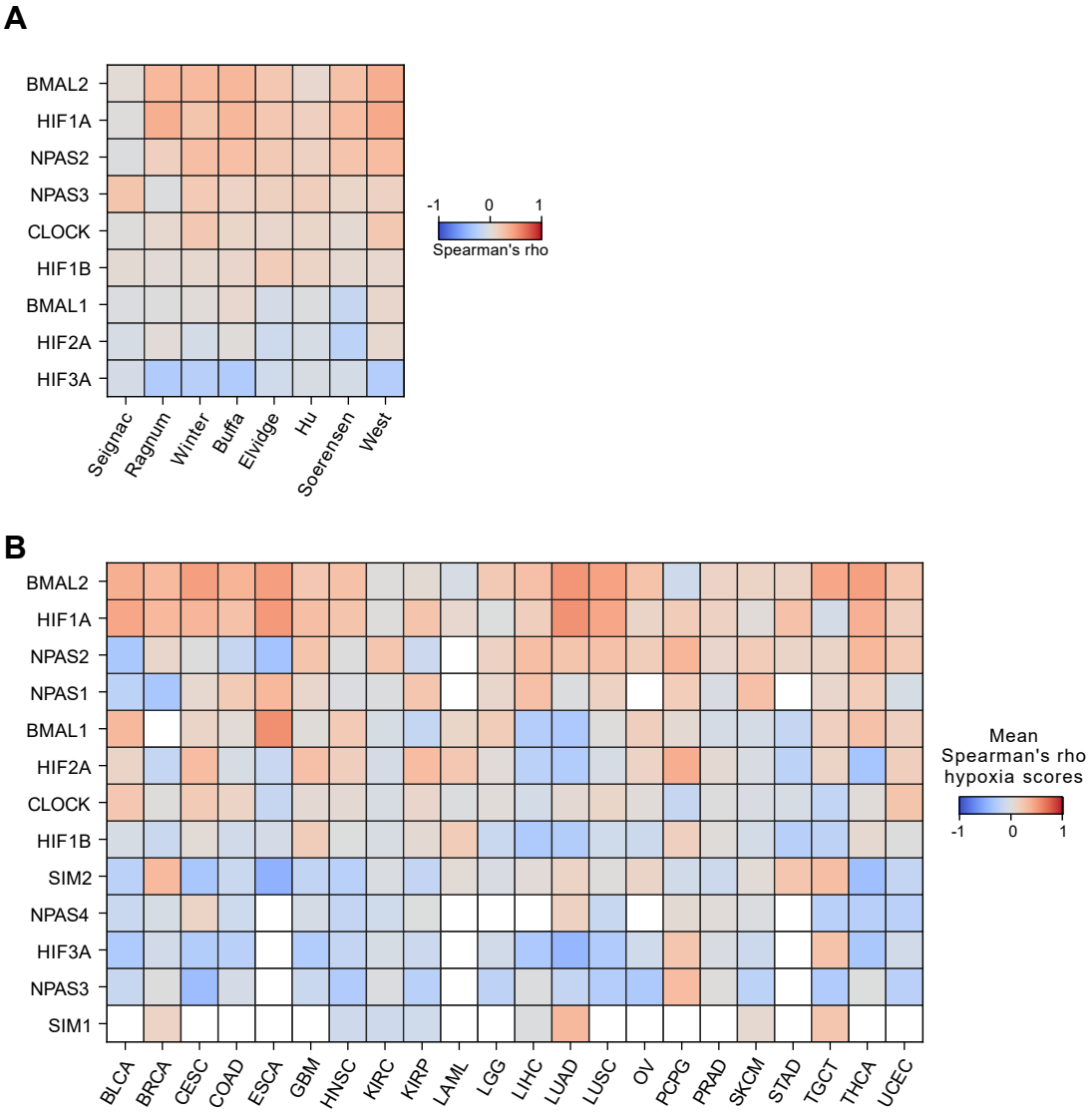

Supplementary Figure 3. (**A**) Heatmap of Spearman's rank correlation between transcriptional hypoxia scores using signatures from the indicated references (x-axis) and stromal protein activity for bHLH-PAS family members (y-axis). (**B**) Heatmap of the average Spearman's rank correlation between eight transcriptional hypoxia scores in the indicated TCGA tumor cohorts (x-axis) and protein activity for bHLH-PAS family members (y-axis)

Supplementary Figure 4

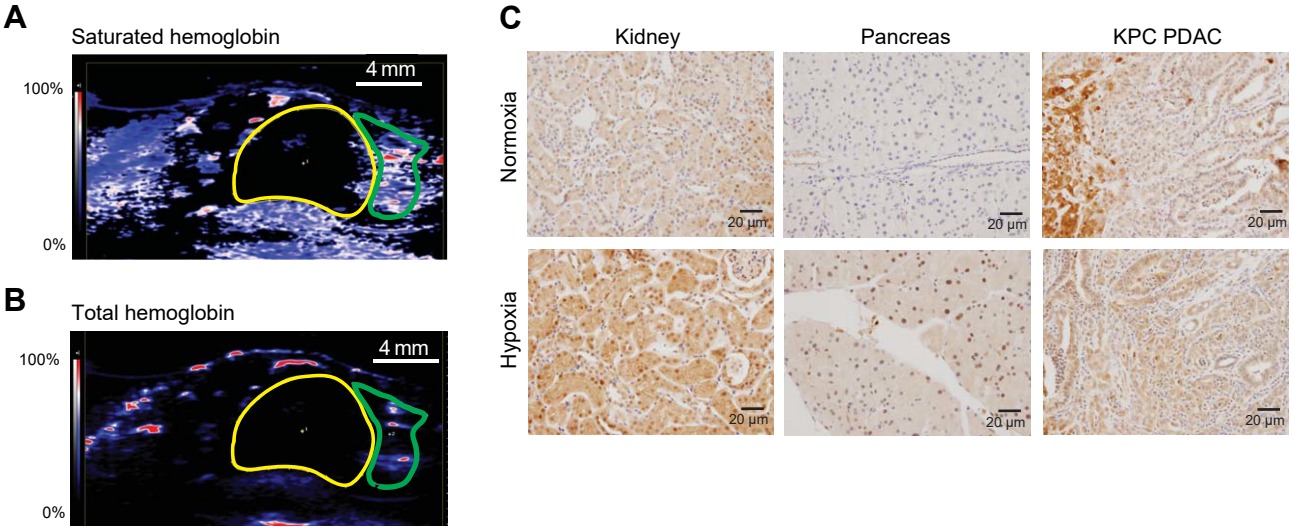

Supplementary Figure 4. (**A**) Heatmap of photoacoustic data from a representative KPC tumor, where red indicates high % blood oxygenation and blue represents low % blood oxygenation. Based on anatomical data from a co-registered B-mode image (not shown), tumor is outlined in yellow and adjacent normal pancreas is outlined in green. (**B**) Heatmap of total hemoglobin content from a representative KPC tumor (yellow) and adjacent normal pancreas (green). (**C**) Anti-pimonidazole (hydroxprobe) IHC stainings of FFPE blocks of normal kidney (left), normal pancreas (middle) and KPC tumors (right) are shown from mice under normoxic (top) or hypoxic (bottom) conditions.